



Quenching or Bursting: The Role of Stellar Mass, Environment, and Specific Star Formation Rate to $z \sim 1$

Behnam Darvish¹ , Christopher Martin¹, Thiago S. Gonçalves², Bahram Mobasher³,
Nick Z. Scoville¹ , and David Sobral^{4,5}

¹ Cahill Center for Astrophysics, California Institute of Technology, 1216 East California Boulevard, Pasadena, CA 91125, USA; bdarv@caltech.edu

² Observatorio do Valongo, Universidade Federal do Rio de Janeiro, Ladeira Pedro Antonio, 43, Saude, Rio de Janeiro-RJ 20080-090, Brazil

³ University of California, Riverside, 900 University Avenue, Riverside, CA 92521, USA

⁴ Department of Physics, Lancaster University, Lancaster, LA1 4 YB, UK

⁵ Leiden Observatory, Leiden University, P.O. Box 9513, NL-2300 RA Leiden, The Netherlands

Received 2017 November 21; revised 2017 December 29; accepted 2018 January 3; published 2018 February 1

Abstract

Using a novel approach, we study the quenching and bursting of galaxies as a function of stellar mass (M_*), local environment (Σ), and specific star formation rate (sSFR) using a large spectroscopic sample of $\sim 123,000$ *GALEX*/SDSS and ~ 420 *GALEX*/COSMOS/LEGA-C galaxies to $z \sim 1$. We show that out to $z \sim 1$ and at fixed sSFR and local density, on average, less massive galaxies are quenching, whereas more massive systems are bursting, with a quenching/bursting transition at $\log(M_*/M_\odot) \sim 10.5\text{--}11$ and likely a short quenching/bursting timescale ($\lesssim 300$ Myr). We find that much of the bursting of star formation happens in massive ($\log(M_*/M_\odot) \gtrsim 11$), high-sSFR galaxies ($\log(\text{sSFR}/\text{Gyr}^{-1}) \gtrsim -2$), particularly those in the field ($\log(\Sigma/\text{Mpc}^{-2}) \lesssim 0$) and, among group galaxies, satellites more than centrals. Most of the quenching of star formation happens in low-mass ($\log(M_*/M_\odot) \lesssim 9$), low-sSFR galaxies ($\log(\text{sSFR}/\text{Gyr}^{-1}) \lesssim -2$), in particular those located in dense environments ($\log(\Sigma/\text{Mpc}^{-2}) \gtrsim 1$), indicating the combined effects of M_* and Σ in the quenching/bursting of galaxies since $z \sim 1$. However, we find that stellar mass has stronger effects than environment on the recent quenching/bursting of galaxies to $z \sim 1$. At any given M_* , sSFR, and environment, centrals are quencher (quenching faster) than satellites in an average sense. We also find evidence for the strength of mass and environmental quenching being stronger at higher redshift. Our preliminary results have potential implications for the physics of quenching/bursting in galaxies across cosmic time.

Key words: galaxies: evolution – galaxies: groups: general – galaxies: high-redshift – galaxies: star formation – large-scale structure of universe – ultraviolet: galaxies

1. Introduction

What causes galaxies to stop forming stars—to quench—is still an unsolved problem in studies of galaxy formation and evolution. Several external and internal mechanisms with different quenching timescales have been proposed, such as ram-pressure stripping, viscous stripping, thermal evaporation, strangulation, galaxy–galaxy interactions, galaxy harassment, mergers, galaxy–cluster tidal interactions (see the review by Boselli & Gavazzi 2006), halo quenching (Birnboim & Dekel 2003), active galactic nucleus (AGN) feedback (see the review by Fabian 2012), stellar feedback (Hopkins et al. 2014), and morphological quenching and secular processes (Sheth et al. 2005; Martig et al. 2009; Fang et al. 2013; Bluck et al. 2014; Nogueira-Cavalcante et al. 2018).

These processes might temporarily enhance star formation in galaxies prior to quenching, or they can cause both negative (quenching) and positive (bursting) feedback. For example, compression of the gas due to thermal instability and turbulent motions and/or the inflow of gas to the center can elevate star formation in galaxies being stripped as a result of ram pressure prior to the full interstellar medium removal of galaxies and hence subsequent quenching (Bekki & Couch 2003; Poggianti et al. 2016, 2017). Galaxy–galaxy interactions might cause the gas in the periphery of the interacting systems to get

compressed and funnel toward the center, triggering a starburst and/or reviving nuclear activity (Mihos et al. 1992; Mihos & Hernquist 1996; Kewley et al. 2006; Ellison et al. 2008, 2013; Sobral et al. 2015; Stroe et al. 2015). AGN feedback can both reduce/stop star formation through quasar- and radio-mode feedback (Best et al. 2005; Croton et al. 2006; Somerville et al. 2008; Hopkins & Elvis 2010; Gürkan et al. 2015) and trigger star formation by compressing gas (by generating cool, dense cavities in the cocoon around the AGN jet; see, e.g., Silk & Nusser 2010; Gaibler et al. 2012; Wagner et al. 2012; Kalfountzou et al. 2017).

More importantly, one particular concern in the study of galaxy evolution is the assumption that galaxies migrate from the blue cloud to the red sequence (i.e., they quench) gradually or quickly, whereas, in principle, they can also burst and rejuvenate as they evolve. For example, using a new method that makes no prior assumption about the star formation history (SFH) of galaxies, Martin et al. (2017) showed that in-transition green valley galaxies in the local universe are both quenching and bursting, although the overall mass flux from the blue cloud to the red sequence is positive (quenching). Therefore, to have a better picture of galaxy formation and evolution, we need to simultaneously study and quantify both the “quenching” and “bursting” of galaxies.

These processes are directly or indirectly associated with the “environment” or “stellar mass” of galaxies, and they often work together in the quenching mechanism (Peng et al. 2010; Quadri et al. 2012; Lee et al. 2015; Darvish et al. 2016; Guo et al. 2017; Henriques et al. 2017; Kawinwanichakij



Original content from this work may be used under the terms of the [Creative Commons Attribution 3.0 licence](https://creativecommons.org/licenses/by/3.0/). Any further distribution of this work must maintain attribution to the author(s) and the title of the work, journal citation and DOI.

et al. 2017; Nantais et al. 2017; Smethurst et al. 2017). The general picture is that “environmental quenching” becomes important at later times (e.g., Peng et al. 2010; Darvish et al. 2016; Hatfield & Jarvis 2017), particularly for less massive galaxies (Peng et al. 2010; Quadri et al. 2012; Lee et al. 2015), and “mass quenching” is more effective on more massive galaxies, especially at higher redshifts (Peng et al. 2010; Lee et al. 2015; Darvish et al. 2016). In groups, environmental quenching is thought to be mostly associated with satellites, whereas mass quenching is mainly linked to centrals (Peng et al. 2012; Kovač et al. 2014; Darvish et al. 2017). However, there are also inconsistencies in the literature on this topic. For example, although some studies point toward an independence of mass quenching and environmental quenching processes (Peng et al. 2010; Quadri et al. 2012; Kovač et al. 2014), others find that they depend on each other (Darvish et al. 2016; Kawinwanichakij et al. 2017). Despite recent progress, the relative importance of environmental and mass quenching, their evolution with cosmic time, and their influence on the physical properties of galaxies are still not fully understood.

In addition to stellar mass and the environment, another parameter that is strongly linked to galaxy quenching is the specific star formation rate (sSFR; SFR/M_*). The inverse of sSFR is a measure of how long it takes a galaxy to assemble its mass given its current SFR. Therefore, it is used to separate star-forming and quiescent systems with a separating sSFR of $\approx 10^{-1}-10^{-2} \text{ Gyr}^{-1}$. The sSFR is tightly coupled to M_* for both star-forming and quiescent systems over a broad redshift range (Noeske et al. 2007; Wuyts et al. 2011; Whitaker et al. 2012; Speagle et al. 2014; Shivaei et al. 2015). The sSFR also depends on the environment and, on average, it is lower in denser regions, particularly at lower redshifts (Peng et al. 2010; Sobral et al. 2011; Scoville et al. 2013; Darvish et al. 2016; Hatfield & Jarvis 2017). However, the cause of lower sSFR in denser environments is still debatable, with some studies only attributing this to a lower fraction of star-forming galaxies in denser regions (Patel et al. 2009; Peng et al. 2010; Koyama et al. 2013; Darvish et al. 2014, 2015a, 2016; Duivenvoorden et al. 2016; Hung et al. 2016; Berti et al. 2017), whereas others link it to both a lower fraction and a lower SFR of star-forming galaxies in denser environments than the field (Vulcani et al. 2010; Patel et al. 2011; Haines et al. 2013; Erfanianfar et al. 2016; Darvish et al. 2017). Nonetheless, the latter studies often find a small reduction of $\sim 0.1-0.3$ dex in star formation activity of star-forming galaxies in denser regions.

In this paper, we investigate both “quenching” and “bursting” of the overall galaxy population, satellite galaxies, and centrals as a function of four main parameters—stellar mass, sSFR, local environment, and redshift since $z \sim 1$ —based on the recent methodology developed by Martin et al. (2017). In Section 2, we introduce the data. The methods used to quantify the environment and the quenching/bursting of galaxies and their properties are developed in Section 3. The results are presented in Section 4, discussed in Section 5, and summarized in Section 6.

Throughout this study, we assume a flat Λ CDM cosmology with $H_0 = 70 \text{ km s}^{-1} \text{ Mpc}^{-1}$, $\Omega_m = 0.3$, and $\Omega_\Lambda = 0.7$ and a Salpeter initial mass function (IMF; Salpeter 1955). As presented in Section 3.3, we define the star formation acceleration (SFA) in units of mag Gyr^{-1} as $\frac{d(\text{NUV} - i)_0}{dt}$, where dt is the past 300 Myr and $(\text{NUV} - i)_0$ is the extinction-corrected NUV $- i$ color, and the star formation jerk (SFJ)

is $\frac{d(\text{NUV} - i)_0}{dt}$, where dt is the past 600–300 Myr. A positive (negative) SFA and SFJ indicate recent quenching (bursting). The SFA (SFJ) uncertainties are estimated as σ/\sqrt{N} , where σ is $1.4826 \times$ the median absolute deviation of the SFA (SFJ) and N is the number of data points.

2. Data and Sample Selection

2.1. Local Universe Sample (SDSS)

The local universe data are from the SDSS DR12 (Alam et al. 2015). Following Baldry et al. (2006), we select galaxies with a clean Galactic extinction-corrected Petrosian magnitude of $r \leq 17.7$ (after excluding stars) and clean spectra (after removing duplicates) in the spectroscopic redshift range of $0.02 \leq z \leq 0.12$, located in the contiguous northern galactic cap ($130.0 \leq \text{R.A. (deg)} \leq 240.0$ and $0.0 \leq \text{decl. (deg)} \leq 60.0$). We use this sample (sample A) for environmental measure estimations, as it provides a contiguous field with relatively uniform, large spectroscopic coverage and completeness. Our estimation of galaxy properties requires SDSS and *GALEX* photometry (Martin et al. 2005) and a 4000 Å break ($D_n(4000)$) and H δ absorption-line index⁶ (see Section 3.3). Therefore, we match sample A with the *GALEX* All-Sky Survey Source Catalog (Seibert et al. 2012; matching radius of 5"), and the resulting catalog is later matched with the MPA-JHU DR8 catalog (Kauffmann et al. 2003) to retrieve reliable $D_n(4000)$ and H δ (median signal-to-noise ratio (S/N) per pixel > 3). The k -correction recipe of Chilingarian et al. (2010) and Chilingarian & Zolotukhin (2012) is used to estimate the rest-frame colors and magnitudes. The final sample comprises 123,469 sources. Figure 1(a) shows the redshift distribution of the sources. We use this final local universe sample for scientific analysis (Section 4).

The magnitude cut of $r \leq 17.7$ results in a redshift-dependent stellar mass completeness limit. We estimate the mass completeness limit using Pozzetti et al. (2010). We assign a limiting mass to each galaxy that corresponds to the stellar mass the galaxy would have if its apparent magnitude were the same as the magnitude limit of the sample ($r \leq 17.7$). At each redshift, the 90% mass completeness, for instance, is then defined as the stellar mass for which 90% of galaxies have their limiting mass below it. We use this 90% cut and estimate the completeness limit to be $\log(M_*^{\text{comp}}/M_\odot) \sim 10.3$ to $z = 0.12$.

2.2. High-redshift Sample (LEGA-C)

As we already mentioned, we require high-S/N $D_n(4000)$ and H δ absorption features (along with photometric information) to robustly extract galaxy properties. At higher redshifts, the only such large and deep galaxy sample available so far is from the VLT LEGA-C spectroscopic survey (van der Wel et al. 2016) in the COSMOS field (Scoville et al. 2007) at $z \approx 0.6-1.0$. Similar to the SDSS quality, this survey is designed to obtain high-resolution ($R \sim 2500$), high-S/N ($\gtrsim 10$, through 20 hr integration) continuum spectra in the wavelength range of $\sim 6300-8800 \text{ \AA}$ for a large (~ 3200) sample of galaxies at $z \sim 1$ using the VIMOS spectrograph. The primary sample is K -band selected with a redshift-dependent magnitude limit to guarantee the coverage of the

⁶ The role of the SDSS limited fiber size (3") has been discussed in Martin et al. (2007, 2017). Martin et al. (2017) found no significant effect on their results. As a sanity check, we also limit our sample to $z = 0.04-0.12$ and find that our results still hold.

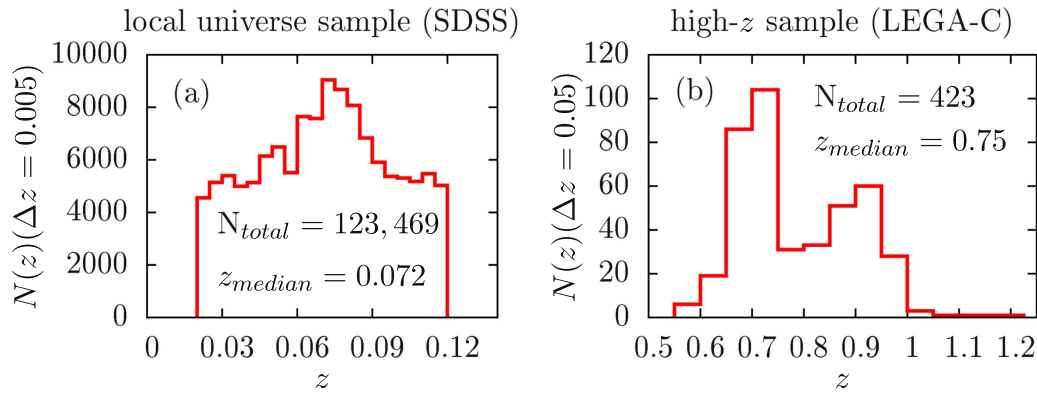


Figure 1. (a) Spectroscopic redshift distribution (in bins of $\Delta z = 0.005$) of our local universe SDSS sample. (b) Spectroscopic redshift distribution (in bins of $\Delta z = 0.05$) of our high- z LEGA-C sample.

full galaxy types, including quiescent, star-forming, and dusty systems at $\log(M_*/M_\odot) \gtrsim 10$ (Chabrier IMF).

We use the LEGA-C first data release (892 spectra) by selecting galaxies with continuum $S/N > 3$ (typical $S/N > 10$) and available $D_n(4000)$ and $H\delta$ indices.⁷ We match this sample with the i^+ -band selected catalog of Capak et al. (2007) to obtain *GALEX* FUV/NUV (Zamojski et al. 2007), *CFHT* u^* , and *Subaru* g^+ , r^+ , and i^+ photometry. We convert the *CFHT* u^* magnitude to the SDSS using $u^* = u - 0.241(u-g)$ (from the *CFHT* website). *Subaru* g^+ , r^+ , and i^+ magnitudes are converted to SDSS using Table 8 in Capak et al. (2007). The k -correction is evaluated using the best-fit spectral energy distribution (SED) template at the redshift of the sources (Ilbert et al. 2009). The final sample contains 423 galaxies spanning $0.6 \lesssim z \lesssim 1.0$ (median redshift of $z_{\text{median}} \approx 0.75$) with a mass completeness limit of $\log(M_*^{\text{comp}}/M_\odot) \sim 10.3$ (van der Wel et al. 2016). Figure 1(b) shows the redshift distribution of our high- z sample.

3. Methods

3.1. Local Environment

There are different measures for defining the “environment” of a galaxy on different physical scales, with each method having its own advantages/disadvantages (see, e.g., Muldrew et al. 2012; Darvish et al. 2015b). These measures include the halo mass, halo size, local overdensity of galaxies, cluster or group membership, distance to the center of the parent halo, cluster, or group, association with different components of the cosmic web, and so on. Throughout this paper, we use the term “environment” or “local environment” to refer to the environment traced by the overdensity of galaxies.

3.1.1. Local Universe

We use the projected comoving distance to the 10th nearest neighbor to each galaxy, considering only galaxies that are within the recessional velocity range of $\Delta v = c\Delta z = \pm 1000 \text{ km s}^{-1}$ to that galaxy, and correct for incompleteness due to the fiber collision and flux limit of the sample,

$$\Sigma_i = \frac{1}{C_i \Psi(z_i)} \frac{10}{\pi d_i^2}, \quad (1)$$

⁷ For both the SDSS and LEGA-C samples, we use the definition of Balogh et al. (1999) in order to extract $D_n(4000)$ and $H\delta$.

where Σ_i is the local projected surface density for the galaxy i , d_i is the projected comoving distance to the 10th neighbor, C_i is a correction term for the galaxy i due to the spectroscopic fiber collision, and $\Psi(z_i)$ is the selection function used to correct the sample for the Malmquist bias.

We evaluate C_i using the Baldry et al. (2006) approach; this is given in Appendix A (see Figure 13). To estimate $\Psi(z_i)$, we follow Efstathiou & Moody (2001) by modeling the change in the number of galaxies (in redshift bins of $\Delta z = 0.005$) as a function of redshift with

$$N(z)dz = Az^2\Psi(z)dz, \quad \text{where } \Psi(z) = e^{-(z/z_c)^\alpha}, \quad (2)$$

A is a normalization factor, and z_c is a characteristic redshift that corresponds to the peak of the redshift distribution. The best-fit model is given by $A = (8.50 \pm 0.75) \times 10^6$, $z_c = 0.0653 \pm 0.0035$, and $\alpha = 1.417 \pm 0.054$ (Figure 14(a), Appendix A). To avoid large uncertainties and fluctuations in the estimated densities due to a smaller sample size at higher redshifts, we only use galaxies for which $\Psi(z) \geq 0.1$ (Figure 14(b), Appendix A). This corresponds to $z \sim 0.12$. For details of the method, why we use the distance to the 10th neighbor, and the selection of $\Delta v = \pm 1000 \text{ km s}^{-1}$, see Appendix A.

3.1.2. High Redshift

We use the density field estimation of Darvish et al. (2017) in the COSMOS field. The local environment measurement relies on the adaptive kernel smoothing method (Scoville et al. 2013; Darvish et al. 2015b) using a global kernel width of 0.5 Mpc estimated over a series of overlapping redshift slices (Darvish et al. 2015b). A mass-complete sample (similar to a volume-limited sample) is used for density estimation. There are several known large-scale structures (LSSs) in the COSMOS field in the redshift range of our sample (e.g., Finoguenov et al. 2007; Guzzo et al. 2007; Sobral et al. 2011; Scoville et al. 2013; Darvish et al. 2014) that provide us with a relatively large dynamical range of environments for our high- z sample at $0.6 \lesssim z \lesssim 1$.

Using different density estimators at low- and high- z (10th nearest neighbor versus adaptive kernel smoothing) might lead to a potential bias in comparing the results at low and high redshift. However, in Appendix B, we compare the density estimation using the 10th nearest neighbor and adaptive kernel smoothing for our high- z sample and find a good agreement. Moreover, Darvish et al. (2015b) found an overall good

agreement between the estimated density fields using different methods (including the 10th nearest neighbor and adaptive kernel smoothing) over ~ 2 dex in overdensity values through simulations and observational data. Hence, the selection of different estimators has no significant effect on the presented results.

3.2. Central and Satellite Selection

3.2.1. Local Universe

We rely on a sample of galaxy groups (in sample A) to select central and satellite galaxies. We select the brightest galaxy in each group as the central and the rest of the group members as satellites. Galaxies that are not related to any galaxy group (isolated galaxies) are either centrals whose satellites are, in principle, too faint to be detected in our sample or ejected satellites moving beyond their halos' virial radius (e.g., Wetzell et al. 2014). Galaxy groups are selected using the friends-of-friends algorithm (Huchra & Geller 1982). Two galaxies i and j with redshifts z_i and z_j , respectively, and angular separation θ_{ij} are linked to each other if their projected ($D_{\perp,ij}$) and line-of-sight ($D_{\parallel,ij}$) separations satisfy the following conditions:

$$\begin{aligned} D_{\perp,ij} &\leq b_{\perp}n(z)^{-1/3}, & D_{\perp,ij} &= \frac{c}{H_0}(z_i + z_j)\sin(\theta_{ij}/2) \\ D_{\parallel,ij} &\leq b_{\parallel}n(z)^{-1/3}, & D_{\parallel,ij} &= \frac{c}{H_0}|z_i - z_j| \end{aligned} \quad (3)$$

where c is the speed of light, H_0 is the Hubble constant, $n(z)$ is the mean number density of galaxies at z (average redshift of galaxies i and j) estimated from Equation (5), and b_{\perp} and b_{\parallel} are the projected and line-of-sight linking lengths in units of the mean intergalaxy separation. Here we use $b_{\perp} = 0.07$ and $b_{\parallel} = 1.1$, proposed by Duarte & Mamon (2014) to be best suited for environmental studies. In Section 4, when we use the term ‘‘all galaxies,’’ we mean all galaxies in our sample (central+satellite+isolated).

3.2.2. High Redshift

We match our high- z sample with the Darvish et al. (2017) catalog of satellites, centrals, and isolated systems in the COSMOS field. Their group selection is similar to that of our local universe sample, but the linking parameters are optimized according to their selection functions. Nonetheless, the fraction of different galaxy types is very similar between the SDSS and COSMOS galaxies, which guarantees a reliable comparison between our low- and high- z samples (15% (16%), 46% (48%), and 39% (36%) for SDSS (COSMOS) centrals, satellites, and isolated systems, respectively).

3.3. Galaxy Physical Properties

3.3.1. Method

Our extraction of galaxy physical properties relies on the Martin et al. (2017) method. It utilizes semi-analytical models (De Lucia et al. 2006) in the context of the cosmological N -body simulation (Springel et al. 2005) to generate a sample of model galaxies at $0 < z < 6$ with known physical parameters such as SFR, stellar mass, and other parameters, including the instantaneous time derivative of the SFR that we denote as the SFA and a similar quantity we denote as the SFJ. Single stellar populations (Bruzual & Charlot 2003) and a simple extinction slab model are then used to convert the SFHs

into observable colors and spectral indices. At each $D_n(4000)$ bin and redshift, a linear regression fit is then performed between the physical parameters and the model observables, resulting in a series of coefficients that are later used to convert the actual observables to the physical parameters for galaxy samples. The observables that we use here are the rest-frame FUV – NUV, NUV – u , u – g , g – r , and r – i colors, rest-frame M_i absolute magnitude, $D_n(4000)$, and $H\delta$:

$$\begin{aligned} P_p(\text{est}) &= C_{1,p,d,z}(\text{FUV} - \text{NUV}) \\ &+ C_{2,p,d,z}(\text{NUV} - u) + C_{3,p,d,z}(u - g) \\ &+ C_{4,p,d,z}(g - r) + C_{5,p,d,z}(r - i) \quad , \quad (4) \\ &+ C_{6,p,d,z}H\delta + C_{7,p,d,z}D_n(4000) \\ &+ C_{8,p,d,z}M_i + \text{CTE}_{p,d,z} \end{aligned}$$

where P is the estimated physical parameter, $C_{i,p,d,z}$ is the coefficient of the observable i for the physical parameter p at a redshift bin of z and $D_n(4000)$ bin of d , and $\text{CTE}_{p,d,z}$ is a constant. If the sources are not detected in the FUV band, we only rely on other observables in determining the physical parameters.⁸

The derived physical parameters that we use in this work are SFA (in units of mag Gyr^{-1} ; defined as $\frac{d(\text{NUV}-i)_0}{dt}$, where dt is the past 300 Myr and $(\text{NUV} - i)_0$ is the extinction-corrected NUV – i color), SFJ (in units of mag Gyr^{-1} ; defined as $\frac{d(\text{NUV}-i)_0}{dt}$, where dt is the past 600–300 Myr), stellar mass M_* , and sSFR. A positive (negative) value of SFA and SFJ indicates quenching (bursting) in the past 300 and 600–300 Myr, respectively. The combination of SFA and SFJ can place constraints on the strength and typical timescale of quenching and bursting.

Martin et al. (2017) compared the derived M_* , SFR, and other physical quantities in the local universe with similar ones in the literature and found a relatively good agreement (within ~ 0.1 – 0.2 dex). For details of the method, potential degeneracies, and comparisons with the literature, see Martin et al. (2017). Some other comparisons can be found in Appendix C of this paper.

3.3.2. SFA and Quenching/Bursting Timescale

In Martin et al. (2017), no prior assumptions are made about the shape of the SFHs used in extracting the physical parameters. This allows us to extract new physical parameters such as SFA. However, in order to give a sense of how the SFA is related to the typical quenching/bursting timescales, we model the changes in NUV – i color with time (used in the SFA definition) assuming an exponentially declining SFH with different e -folding (quenching) timescales (Martin et al. 2007). We assume that the SFR is constant for 5 Gyr, followed by an exponentially declining SFH ($\propto e^{-\frac{t}{\tau}}$) with different τ values. We model the NUV – i color changes (SFA) after the onset of quenching using the Bruzual & Charlot (2003) models, assuming a Salpeter IMF, solar metallicity, and no dust. Figure 2 shows the SFA as a function of quenching timescale τ for this simplistic model. Note that the relation between SFA and τ should be used with caution, given the assumptions used

⁸ This is particularly important, since quiescent galaxies and dusty systems may not have a high enough level of FUV emission to be detected. Hence, exclusion of non-detected FUV sources would automatically bias the analysis to samples with higher sSFR and low dust content.

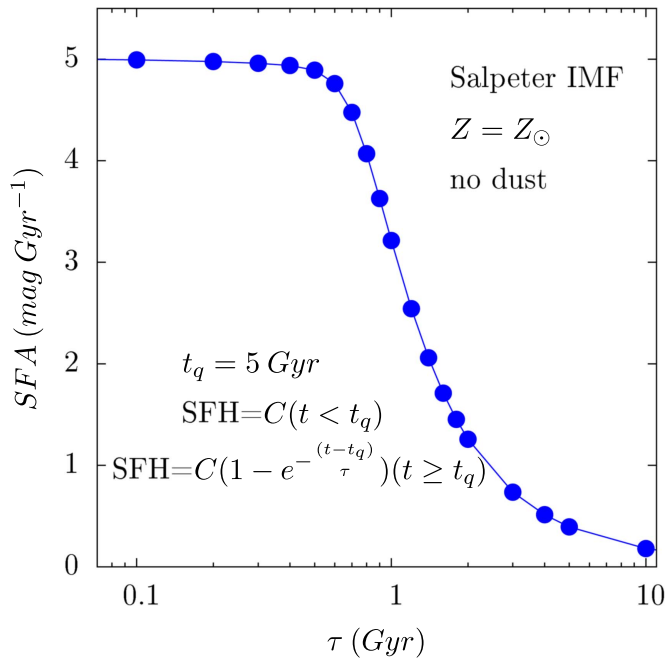


Figure 2. SFA as a function of quenching timescale τ for a constant, 5 Gyr long SFH, followed by an exponentially declining SFH with different quenching timescales τ . Unextinguished models with Salpeter IMF and solar metallicity are used.

here. However, Figure 2 gives us a qualitative impression about the physical meaning of SFA that will be extensively used in the following section.

4. Results

4.1. Quenching/Bursting of Galaxies in the Local Universe

Figure 3(a) shows the SFA as a function of stellar mass for our SDSS sample (black triangles). A positive (negative) value indicates recent quenching (bursting) in the past 300 Myr. We clearly see a trend with stellar mass, in the sense that, on average, less massive galaxies tend to be quenching and more massive systems bursting, consistent with Martin et al. (2017). The transition between quenching and bursting occurs at $\log(M_*/M_\odot) \sim 10.5\text{--}11$. Figure 3(b) shows the SFJ versus stellar mass for our local universe sample. A positive (negative) value indicates past quenching (bursting) at 600–300 Myr prior to observations. We still see a very weak correlation between SFJ and M_* , particularly at $\log(M_*/M_\odot) \gtrsim 11$, but clearly, much of the quenching/bursting has happened recently as seen in Figure 3(a). This indicates that the physics of mass quenching/bursting acts in a relatively short timescale ($\lesssim 300$ Myr).

Figures 3(a) and (b) also show the SFA and SFJ versus M_* for central and satellite galaxies. To minimize the projection and group selection effects and contamination by interlopers, we only consider satellites and centrals that are in groups with >10 members. Satellites follow the general trends between SFA and SFJ versus M_* . Centrals follow the same slope between SFA and M_* . However, centrals tend to avoid the bursting region, and, at a given M_* , centrals are quencher than satellites.

Figures 3(c) and (d) show the role of the local environment (Σ) on the SFA and SFJ. When averaged over all stellar masses, we find no clear trend (at best a weak correlation) between SFA (or SFJ) and Σ . Except for an increasing SFJ for centrals in dense regions, satellites and centrals do not show

any significant environmental dependence in their very recent (<300 Myr) and less recent (past 300–600 Myr) quenching/bursting, as denoted by SFA and SFJ quantities (when averaged over all stellar masses). This indicates that the local environment likely acts effectively on a much longer timescale when averaged over all M_* . There are other possibilities too. For example, the local environment might not affect the quantities that are linked to the quenching/bursting of galaxies. It might also be due to the mass quenching/bursting being more effective than the environmental quenching/bursting when averaged over the general population of galaxies.

We further investigate the quenching/bursting of galaxies by dividing our sample into stellar mass, sSFR, and density bins. Figure 4 shows the median SFA and SFJ (shown by color) on the $\log \Sigma$ versus $\log(M_*/M_\odot)$ plane for all galaxies, satellites, and centrals. The top number in each cell is the median value, and the bottom one is its uncertainty. The mass dependence of SFA is clearly seen on the $\log \Sigma$ versus $\log(M_*/M_\odot)$ diagram, in the sense that in any given environment, more massive systems are burstier than less massive galaxies. However, the local environmental dependence of SFA is also evident. In each mass bin, on average, denser environments host higher quenchedness than the less dense field. The largest burstiness occurs in massive field galaxies ($\log(M_*/M_\odot) \gtrsim 11.5$ and $\log \Sigma \lesssim 0$), and the largest quenchedness belongs to low-mass systems in very dense environments ($\log(M_*/M_\odot) \lesssim 9.0$ and $\log \Sigma \gtrsim 0.5$).

In addition, at fixed Σ , the SFA change with stellar mass is stronger than the SFA change with environment while fixing M_* . In other words, although the SFA depends on both stellar mass and environment, the stellar mass dependence is stronger. Also note that the environmental dependence of SFA is less significant in the medium range of stellar masses ($\log(M_*/M_\odot) \approx 9.5\text{--}11$), and that is why, on average, we do not find a significant environmental dependence of SFA in Figure 3.

The median SFA of satellites follows the general distribution of galaxies, and it depends on both stellar mass and environment. However, the SFA of centrals only shows a mass dependence, and, within the uncertainties, it is almost independent of the local environment (or at best has a weak dependence). This suggests that the environmental dependence of SFA is mostly due to satellites.

Note that in each stellar mass and environment bin, centrals are quencher than satellites, and centrals are mainly quenching. Compared to the SFA, the SFJ shows much weaker dependence on M_* and almost no (or at best a weak) environmental dependence.

The strong sSFR dependence of the trends investigated so far is also evident in Figures 5 and 6. Figure 5 shows the median SFA and SFJ on the diagram of $\log(\text{sSFR})$ versus $\log(M_*/M_\odot)$ for all galaxies, satellites, and centrals at $z \sim 0$. The mass dependence of SFA is also seen on the $\log(\text{sSFR})$ versus $\log(M_*/M_\odot)$ diagram; i.e., at fixed sSFR and on average, more massive galaxies are burstier than less massive systems. However, the SFA strongly depends on sSFR as well. At fixed stellar mass and on average, the median SFA increases with decreasing sSFR, confirming the M_* -sSFR trend seen in Martin et al. (2017) for “all galaxies.” In fact, the burstiness occurs in massive star-forming galaxies with high sSFRs ($\log(\text{sSFR})(\text{Gyr}^{-1}) \gtrsim -3$).

Similar trends are seen for satellites and centrals; that is, on average, the SFA increases with decreasing stellar mass and sSFR for both satellites and centrals. However, in each M_* and sSFR bin, centrals quench faster than (or at best have similar

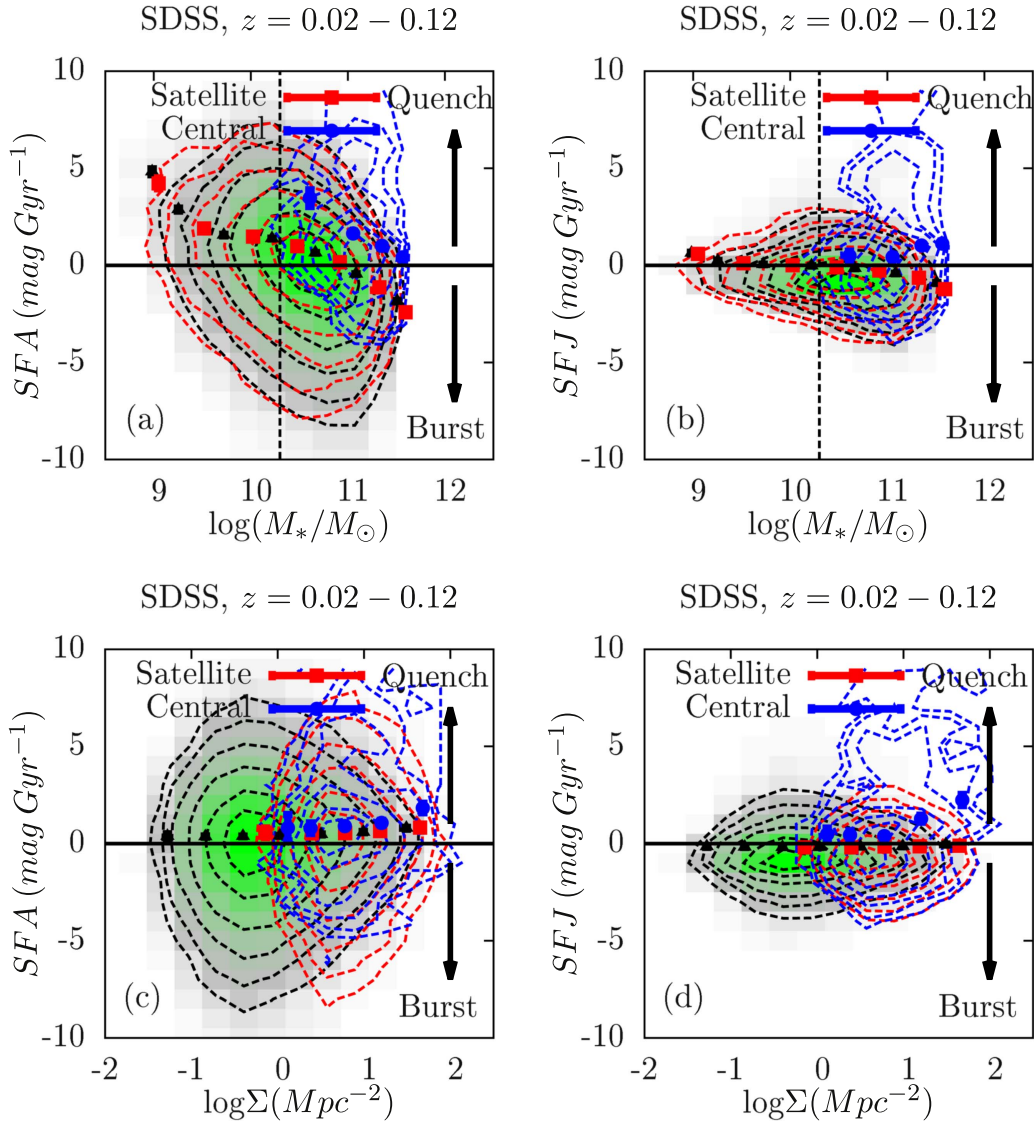


Figure 3. (a) Median SFA as a function of stellar mass for all (black triangles), satellite (red squares), and central (blue circles) galaxies in the local universe. The overall distribution of SFA vs. M_* is shown as a heat map. Black, red, and blue contours correspond to all, satellite, and central galaxies, respectively. Contour levels are at $3/4$, $1/2$, $1/4$, $1/8$, $1/16$, and $1/32$ of the peak. The black vertical line shows the stellar mass completeness limit. A positive (negative) SFA value indicates recent quenching (bursting) in the past 300 Myr. On average, less massive galaxies tend to be quenching and more massive systems bursting with a transition at $\log(M_*/M_\odot) \sim 10.5$ – 11 . Satellites follow the general trends between SFA and M_* . Centrals avoid the bursting region and, at a given M_* , are quencher than satellites. (b) Similar to (a) but for SFJ vs. M_* . A positive (negative) value indicates quenching (bursting) at 600–300 Myr prior to observations. A very weak correlation between SFJ and M_* is seen. (c) Median SFA as a function of local density for all, satellite, and central galaxies in the local universe, with no (or a weak) environmental dependence when averaged over all stellar masses. (d) Similar to (c) but for SFJ vs. $\log \Sigma$.

SFA to) satellites. Compared to the SFA, the SFJ shows weaker dependence on M_* and sSFR (or at best similar values in massive, low-sSFR galaxies).

Finally, the SFA and SFJ as a function of sSFR and local density is shown in Figure 6. At a fixed environment, the median SFA depends on sSFR and increases with decreasing sSFR. However, at a fixed sSFR and within the uncertainties, the median SFA is almost independent of the local density of galaxies. These results hold for all galaxies, as well as satellites and centrals. The weaker sSFR and Σ dependence of the SFJ compared to the SFA is also seen. Combining the results in Figures 4–6 indicates that at $z \sim 0$, much of the bursting of star formation happens in massive, high-sSFR galaxies, particularly those in the field (and among group galaxies, satellites more than centrals), whereas most of the quenching of star formation happens in less massive, low-sSFR galaxies, in particular those

located in dense environments. For centrals, quenching is significant even in higher-mass systems.

4.2. Quenching/Bursting of Galaxies at High z

We find similar results at $z \sim 1$ for our LEGA-C sample as shown in Figures 7–10. To increase the statistics, all satellites and centrals (with a number of group members ≥ 2) are included.⁹ Also note the smaller dynamical range of the environment and M_* probed here compared to that of the SDSS. Even with these limitations, some trends between the SFA (and to a smaller degree the SFJ) and M_* , sSFR, and

⁹ However, we note that because of this selection, the high- z group galaxies are more prone to contamination by interlopers. However, in Appendix D, we show that the overall trends are still retrieved (with larger uncertainties) using groups with >10 members.

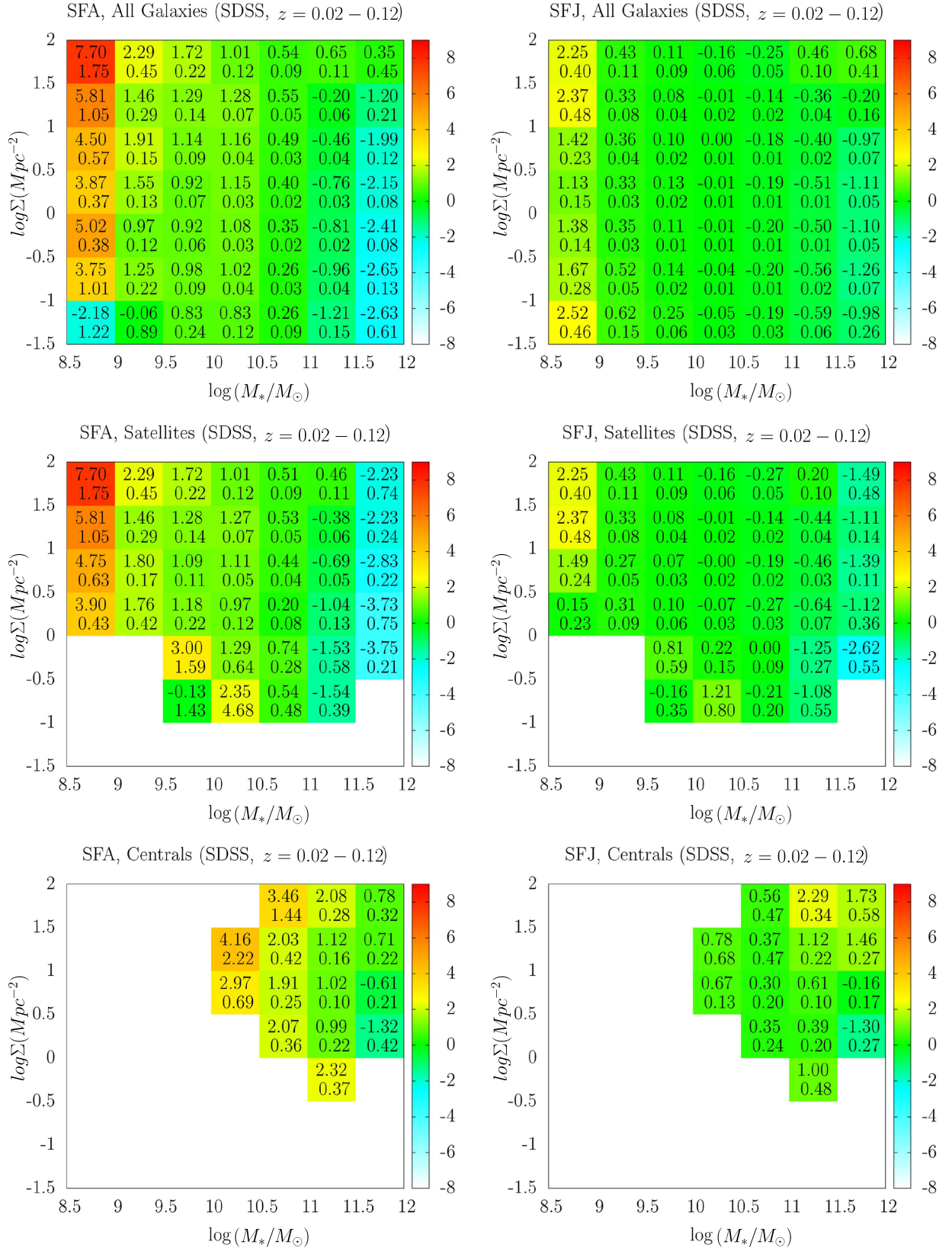


Figure 4. Median SFA (left) and SFJ (right) shown by color on the diagram of $\log \Sigma$ vs. $\log(M_*/M_\odot)$ for all galaxies (top), satellites (middle), and centrals (bottom) in our SDSS sample at $z \sim 0$. The top number in each cell is the median value (SFA or SFJ), and the bottom one is its uncertainty. In each environment, more massive systems are burstier than less massive ones. The local environmental dependence of SFA is also evident; i.e., in each mass bin and on average, denser environments host higher quenchedness than the less dense field. Note that although the SFA depends on both M_* and Σ , the stellar mass dependence is stronger. Also note that the environmental dependence of SFA is less significant in the medium range of stellar masses ($\log(M_*/M_\odot) \approx 9.5-11$). The SFA of satellites also depends on both M_* and Σ . The SFA of centrals only shows a mass dependence, and, within the uncertainties, it is almost independent of the local environment (or at best has a weak dependence). Note that in each stellar mass and local environment bin, centrals are quenched than satellites in an average sense, and centrals are mainly quenched. Compared to the SFA, the SFJ shows much weaker dependence on stellar mass and almost no (or at best a weak) environmental dependence.

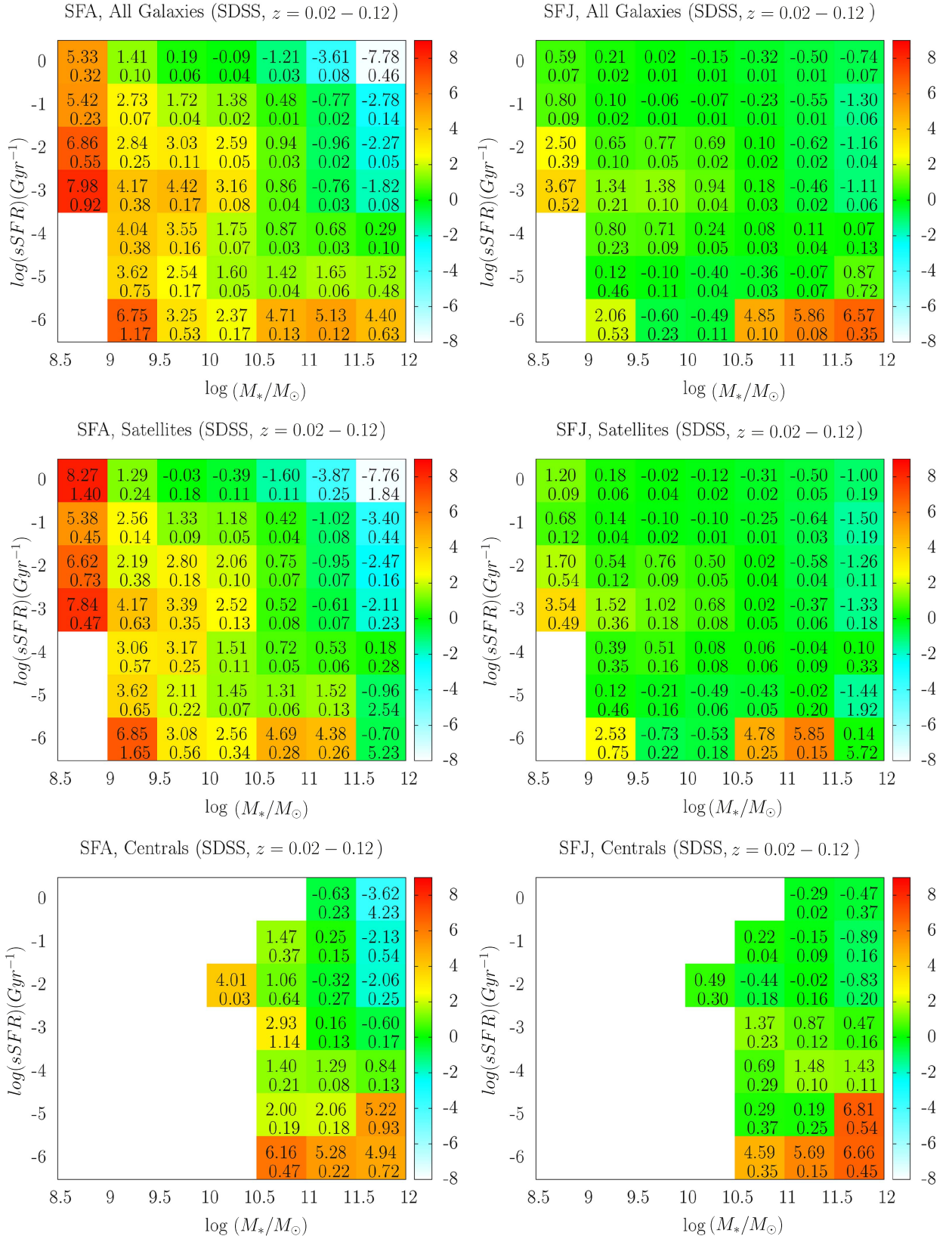


Figure 5. Median SFA (left) and SFJ (right) shown by color on the diagram of $\log(\text{sSFR})$ vs. $\log(M_*/M_\odot)$ for all galaxies (top), satellites (middle), and centrals (bottom) in our SDSS sample at $z \sim 0$. The top number in each cell is the median value (SFA or SFJ), and the bottom one is its uncertainty. At fixed sSFR and on average, less massive galaxies are quenchier than more massive systems. The SFA strongly depends on sSFR as well. At fixed stellar mass and on average, the median SFA increases with decreasing sSFR. The burstiness happens in massive star-forming galaxies ($\log(M_*/M_\odot) \gtrsim 11$) with high sSFR values ($\log(\text{sSFR})(\text{Gyr}^{-1}) \gtrsim -3$). On average, the SFA decreases with increasing M_* and sSFR for satellites and centrals as well. However, in each M_* and sSFR bin, centrals are quenchier than (or have similar SFA to) satellites. Compared to the SFA, the SFJ shows weaker dependence on M_* and sSFR (or at best similar values in massive, low-sSFR galaxies).

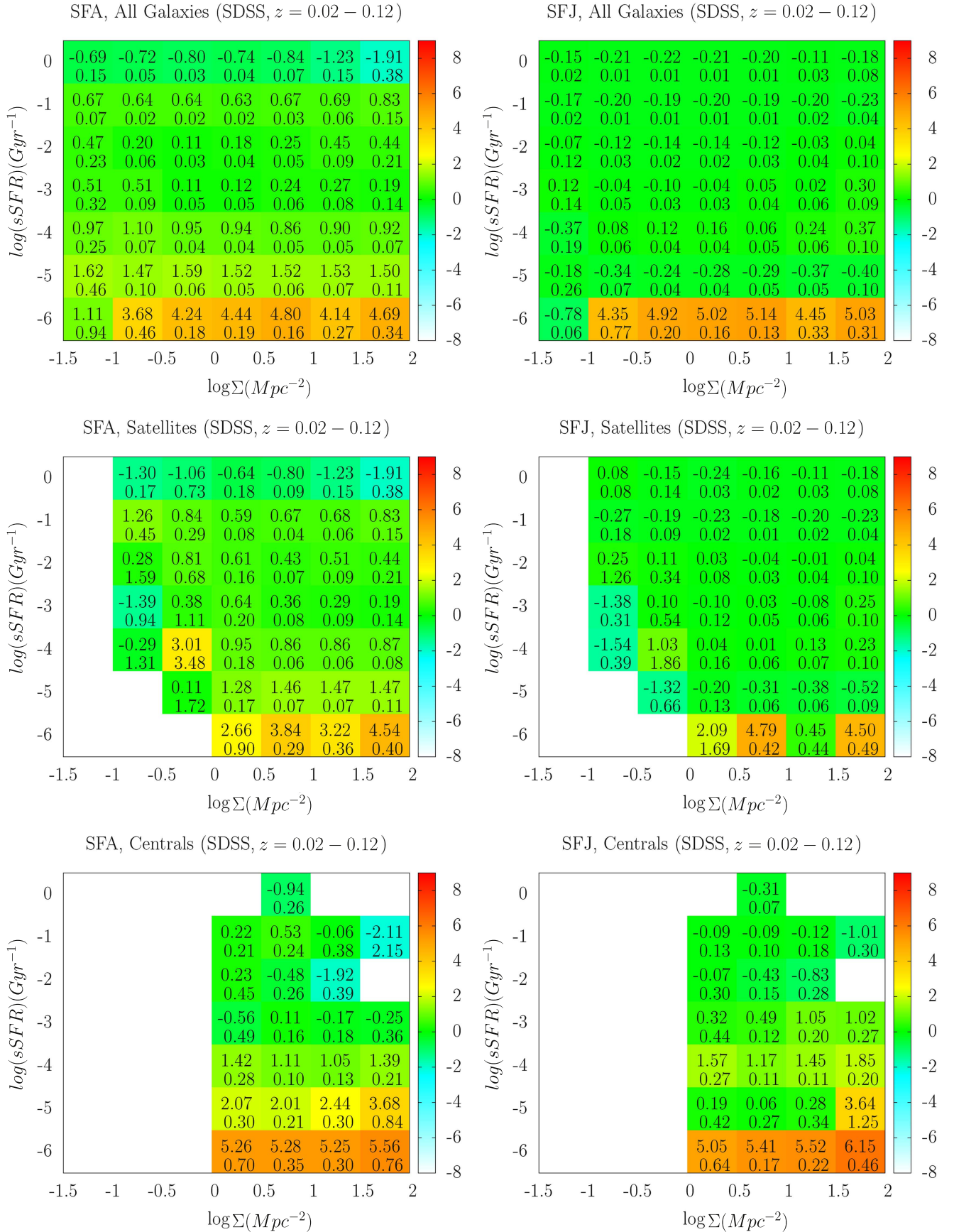


Figure 6. Median SFA (left) and SFJ (right) shown by color on the plane of $\log(sSFR)$ vs. $\log \Sigma$ for all galaxies (top), satellites (middle), and centrals (bottom) in our SDSS sample at $z \sim 0$. The top number in each cell is the median value (SFA or SFJ), and the bottom one is its uncertainty. At a fixed environment, the median SFA depends on sSFR and increases with decreasing sSFR. However, at a fixed sSFR and within the uncertainties, the median SFA is almost independent of Σ . These results hold for all galaxies, satellites, and centrals. The weaker sSFR and Σ dependence of the SFJ compared to the SFA is also seen.

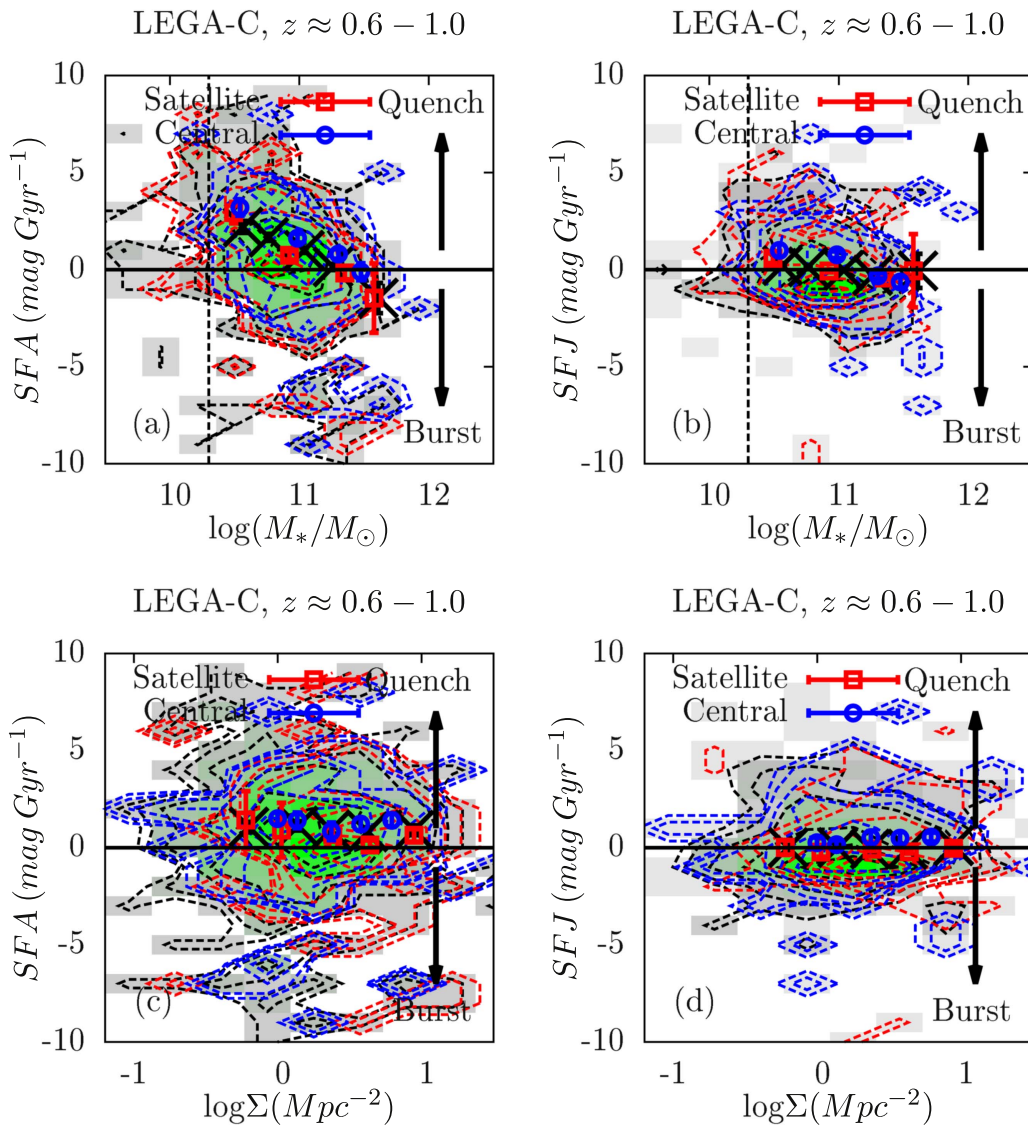


Figure 7. Similar to Figure 3 but for our LEGA-C high- z sample at $z \sim 1$. Red, blue, and black points show the median values for satellite, central, and all galaxies. Similar to the SDSS results, SFA (and SFJ to a lesser degree) decreases with increasing M_* for all galaxies, satellites, and centrals, with evidence for centrals being quencher than satellites at fixed M_* . We also find an environmental independence (when averaged over all the masses and out to $\log \Sigma \sim 1$) of the SFA and SFJ at $z \sim 1$, similar to our results in the local universe.

to a lesser degree environment are evident (with evidence of deviation between centrals and satellites). For example, as shown in Figure 7, we find a mass dependence and an environmental independence (when averaged over all M_* s and to $\log \Sigma \sim 1$) of the SFA and SFJ at $z \sim 1$, with centrals being quencher than satellites, on average.

According to Figure 8, the decrease in median SFA with stellar mass (even at fixed environment) is also seen at $z \sim 1$. Unfortunately, due to a smaller dynamical range of Σ , M_* , and sample size and larger uncertainties in our high- z sample compared to the local universe, we cannot make a significantly robust statement about the potential SFA relation with environment (at a given stellar mass). However, even with these limitations, the overall sample of galaxies shows signs of increasing SFA (and quenching) in denser environments at fixed M_* . The stellar mass dependence of SFA is also seen for both satellites and centrals at $z \sim 1$, but, within the

uncertainties and in the stellar mass and environment range covered at high- z , no clear relation between SFA and environment is seen when we further break the sample into centrals and satellites. Note that even at $z \sim 1$, centrals seem to be quencher than satellites in an average sense. Similar to the low- z results, the SFJ shows weaker M_* and Σ dependence (if any) than the SFA. More importantly, we find that at given bins of stellar mass and environment, higher- z galaxies are, on average, quencher than (or, within the uncertainties, have at best similar SFAs to) their local universe counterparts.

Similar to Figure 5, the median SFA decreases with increasing stellar mass and (to a lesser degree) sSFR for all galaxies, satellites, and centrals at $z \sim 1$. Moreover, at any given stellar mass and sSFR, higher-redshift galaxies (all, centrals, and satellites) are on average quencher than (or, within the uncertainties, have similar SFAs to) their local universe counterparts. Similar to the low- z results, the SFJ

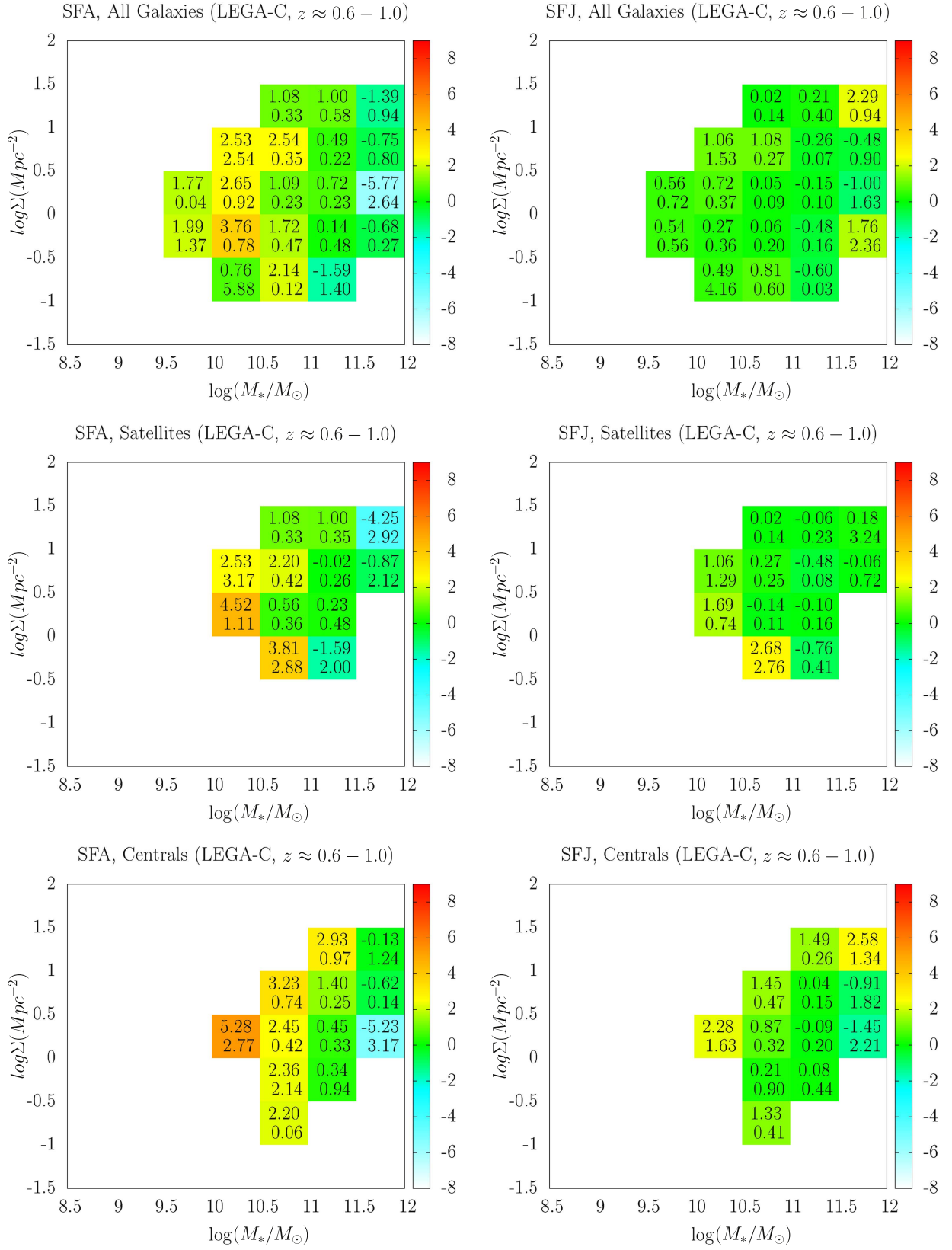


Figure 8. Similar to Figure 4 but for our LEGA-C sample at $z \sim 1$. The median SFA decreases with increasing stellar mass (even at fixed environment) at $z \sim 1$. Unfortunately, due to a smaller dynamical range of environment, stellar mass, and sample size and larger uncertainties in our high- z sample compared to the local universe, we cannot make a significantly robust statement about the potential SFA relation with environment (at a given stellar mass). The overall sample of galaxies shows signs of increasing SFA (and quenching) in denser environments at fixed M_* . However, because of a smaller dynamical range of Σ , M_* , and sample size and larger uncertainties than the low- z sample, we cannot make a robust statement on the potential environmental dependence of SFA (at a given stellar mass) at $z \sim 1$. The stellar mass dependence of SFA is also seen for both satellites and centrals at $z \sim 1$ but within the uncertainties, and, in the M_* and Σ range covered at high z , no clear relation between SFA and environment is seen for satellites. Even at $z \sim 1$, centrals are quenched than satellites, on average. Similar to the SDSS results, the SFJ shows weaker dependence on M_* and Σ (if any) than the SFA.

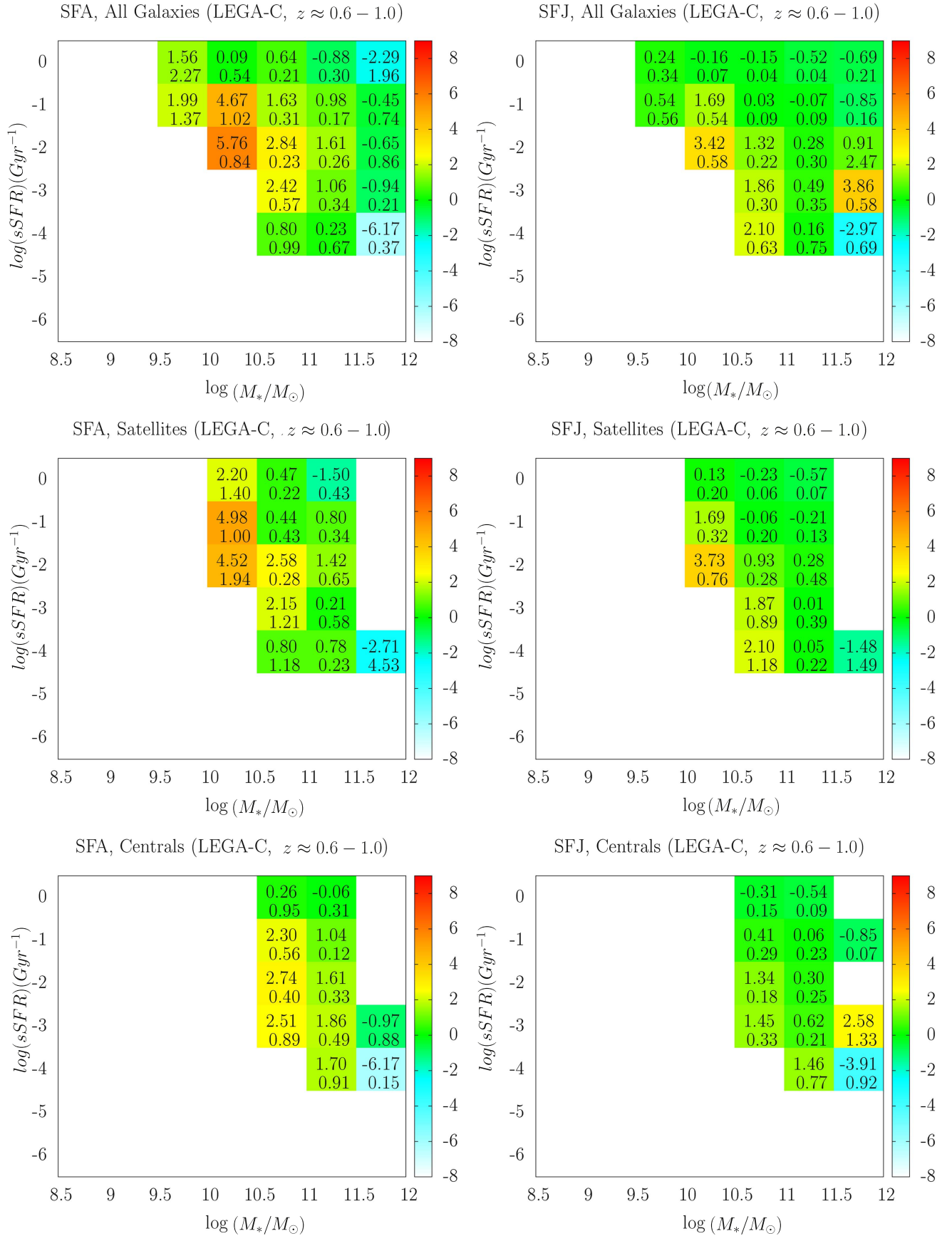


Figure 9. Similar to Figure 5 but for our high- z LEGA-C sample at $z \sim 1$. Similar to the low-redshift results, the median SFA decreases with increasing stellar mass and sSFR for all galaxies, satellites, and centrals. Similarly, the SFJ shows weaker (or similar) dependence on stellar mass and sSFR than the SFA.

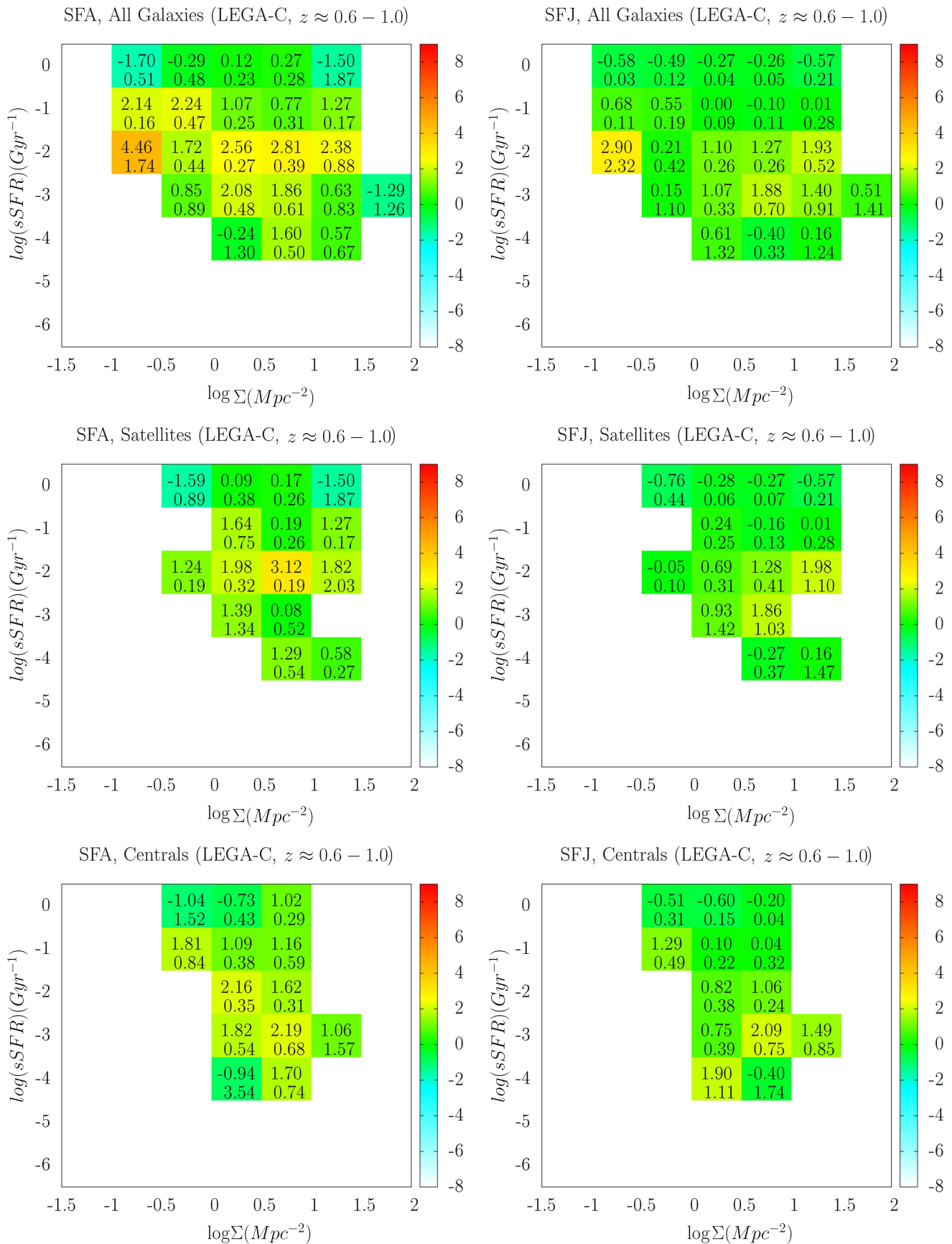


Figure 10. Similar to Figure 6 but for our sample at $z \sim 1$. Given the small range of environments and sSFRs and large uncertainties, no significant trend between SFA and environment or sSFR is seen here. However, some environmental bins show signs of an increasing SFA with decreasing sSFR, similar to the SDSS results. At fixed sSFR and Σ , the SFJ shows smaller values than (or similar values to) the SFA.

shows weaker (or similar) trends with M_* and sSFR than the SFA. Given the narrow range of environments and sSFRs and large uncertainties, no significantly clear trend between SFA and environment or sSFR is seen in Figure 10. However, some environmental bins show signs of an increasing SFA with decreasing sSFR, similar to the results at low z . Moreover, at any given Σ and sSFR, higher- z galaxies (all, centrals, and satellites) are, on average, quencher than (or, within the uncertainties, have similar SFAs to) their local universe counterparts. At fixed sSFR and Σ , the SFJ shows smaller values than (or similar values to) the SFA.

In selecting the group galaxies for the high- z sample, all groups with ≥ 2 members are considered. This makes the sample more prone to contamination by interlopers and might lead to unwanted biases when we compare the low- and high- z results. However, in Appendix D, we show that the global trends could still be recovered using groups with > 10 members for the high- z sample.

4.3. Redshift Evolution of Galaxy Quenching/Bursting

Comparing the low- and high- z results indicates that at fixed M_* , sSFR, and environment, higher-redshift galaxies (all, centrals, and satellites) are, on average, quencher than their local universe counterparts. This is more clearly seen in Figure 11. At fixed M_* (averaged over all environments and sSFRs; top panels), fixed sSFR (averaged over Σ and M_* ; bottom panels), and more slightly at fixed Σ (averaged over sSFR and M_* middle panels), on average, our high- z sample is quencher than the local universe sample.

To further quantify the redshift evolution of the mass and environmental quenching and potentially compare their relative strength, we define the quantity $\Delta_{\text{SFA}} = |\text{SFA}(z \sim 1) - \text{SFA}(z \sim 0)|$ as the absolute difference between the median SFA at $z \sim 1$ (LEGA-C sample) and at $z \sim 0$ (SDSS sample). We define a similar quantity for the SFJ ($\Delta_{\text{SFJ}} = |\text{SFJ}(z \sim 1) - \text{SFJ}(z \sim 0)|$). This absolute difference is done as a function of both stellar mass and environment and at the common stellar mass and environmental range of values for the high- z and local universe samples ($\log(M_*/M_\odot) \approx 10\text{--}12$ and $\log(\Sigma) \approx -0.25\text{--}1.5$). We model the median SFA (and SFJ) as a function of M_* and Σ with linear functions, taking their uncertainties into account. The absolute difference defined in Δ represents the difference between the linearly modeled SFA (or SFJ). Figure 12 shows the results. Both stellar mass and environment show stronger strength in recent quenching/bursting of galaxies at higher redshift. Moreover, the change in stellar mass quenching/bursting seems to be larger ($\Delta_{\text{SFA}}(M_*) \approx 1.7\text{--}0.8 \text{ mag Gyr}^{-1}$ at $10 \lesssim \log(M_*/M_\odot) \lesssim 12$) than the environment ($\Delta_{\text{SFA}}(\Sigma) \approx 0.4\text{--}0.1 \text{ mag Gyr}^{-1}$ at $0.5 \lesssim \log(\Sigma) \lesssim 1.5$) since $z \sim 1$. The SFJ shows weaker trends compared to the SFA.

5. Discussion

To $z \sim 1$, we find that (1) the SFA (and SFJ to a lesser degree) decreases with increasing stellar mass, increasing sSFR, and decreasing local density; (2) on average, centrals quench faster than satellites; and (3) high-redshift galaxies are quencher than their local universe counterparts.

To explain the mass dependence of SFA, Martin et al. (2017) proposed a scenario in which lower-mass galaxies accrete into halos and become satellites, having their star-forming gas

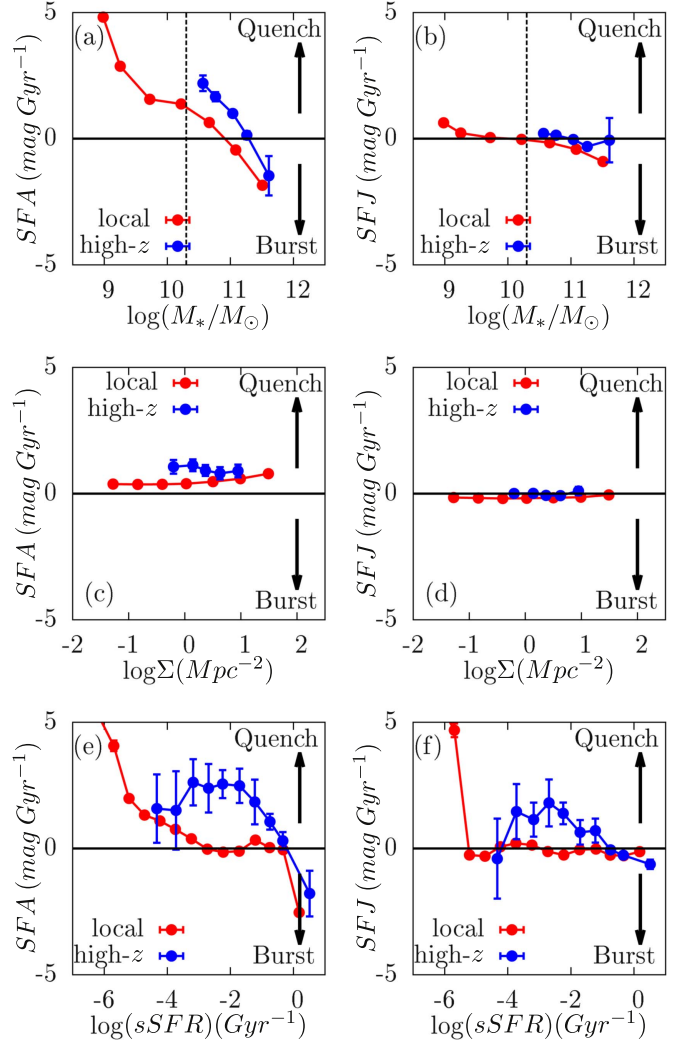


Figure 11. (a) Median SFA vs. M_* , (b) SFJ vs. M_* , (c) SFA vs. $\log \Sigma$, (d) SFJ vs. $\log \Sigma$, (e) SFA vs. sSFR, and (f) SFJ vs. sSFR for our local universe and high- z samples. On average, at fixed M_* , sSFR, and (to a lesser degree) Σ , the higher-redshift galaxies are quencher. The black vertical line shows the stellar mass completeness limit.

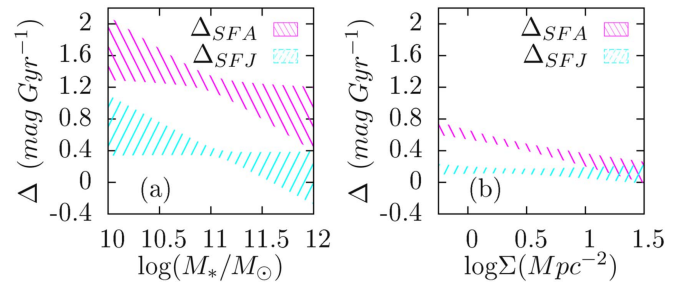


Figure 12. The $\Delta_{\text{SFA}} = |\text{SFA}(z \sim 1) - \text{SFA}(z \sim 0)|$ and $\Delta_{\text{SFJ}} = |\text{SFJ}(z \sim 1) - \text{SFJ}(z \sim 0)|$ as a function of (a) stellar mass and (b) local environment. Here Δ is defined to investigate the redshift evolution of mass and environmental quenching/bursting. The Δ_{SFA} (and to a lesser degree Δ_{SFJ}) values show that the strength of the recent mass and environmental quenching/bursting is larger at higher redshift.

tidally and/or ram-pressure stripped, while higher-mass centrals receive the gas and react with new star formation. However, by explicitly breaking the sample into satellites and

centrals, we see the opposite trend, with centrals being quenched than satellites at fixed M_* , sSFR, and Σ bins in an average sense out to $z \sim 1$.

Wet mergers can boost star formation due to gas compression in short timescales, followed by subsequent quenching over a longer timescale due to gas consumption and the potential rejuvenation of the nuclear activity in merging systems (e.g., Mihos & Hernquist 1996; Ellison et al. 2008, 2013; Mortazavi et al. 2018). There is also evidence for the merger rate being higher for more massive systems (e.g., Patton & Atfield 2008; Xu et al. 2012; Robotham et al. 2014). Therefore, the merger scenario can potentially explain the fast bursting of star formation for massive, high-sSFR star-forming galaxies. The merger picture might also explain why centrals are quenching faster than satellites, if the dominant wet mergers in centrals had happened much earlier than that of satellites, so that at present, we are mainly witnessing the quenching phase of the merger. An even older (>600 Myr) star formation derivative might reveal the past bursting phase of centrals. Moreover, whether the wet merger is “major” or “minor” might also explain why centrals are quenching faster than satellites. In other words, the current bursting of star formation in massive satellites might be because of wet major mergers, whereas this recent bursting in massive centrals could be mostly due to wet minor mergers.

Although the wet-merger scenario might explain the burstiness of massive galaxies in the field as seen in, e.g., Figure 4 (also see Lin et al. 2010), the merger picture becomes problematic in denser environments. Mergers are more common in denser environments than in the field (especially in group scales; Perez et al. 2009; Sobral et al. 2011; Tonnesen & Cen 2012), but we see in, e.g., Figures 3 and 7 that satellites and the overall galaxy distribution follow similar bursting trends. Moreover, there is evidence that centrals are as old as or even younger than satellites, and they are quenched at the same time as or even more recently than satellites of the same mass (Pasquali et al. 2010; Fitzpatrick & Graves 2015; Smethurst et al. 2017). Moreover, mergers in dense environments seem to be mostly dry, and the merger-driven history of centrals is mainly due to gas-poor, dry mergers with no significant star formation (e.g., McIntosh et al. 2008; Lin et al. 2010; Lidman et al. 2012; Shankar et al. 2015; Davidzon et al. 2016).

By studying SDSS galaxy pairs, Ellison et al. (2010) showed that although interactions happen at all environments, interaction-triggered star formation is seen only in low-to-intermediate-density environments. The position of centrals in the densest regions of groups/clusters is in agreement with this picture and explains why they avoid bursting, especially in the densest regions, as clearly seen in, e.g., Figure 4.

There is evidence for the gas fraction being higher in the field galaxies than in denser environments, as previous accretion of galaxies into their current halos made them gas-stripped (Cortese & Hughes 2009; Fabello et al. 2012; Catinella et al. 2013; Boselli & Gavazzi 2014). It is also possible that the cold gas accretion from the surrounding LSS can more easily/efficiently/numerously penetrate isolated and satellite galaxies than centrals that are located in the densest regions of groups/clusters. Van de Voort et al. (2017)’s simulations show that more massive centrals and satellites both have a higher gas accretion rate than less massive ones (also see Dekel et al. 2013). They also found that the gas accretion rate is lower or fully suppressed (depending on the halo mass) in the

center of halos. They also found a strong environmental dependence of accretion rate, primarily for satellites. This might explain the strong quenching of low-mass satellites in denser regions seen in Figure 4. Therefore, a combination of stellar mass and halocentric and environmental dependence of gas accretion rate, gas fraction, and mergers can potentially explain the observed trends. Further analyses, including gas and age dependence of different galaxy types on SFA, SFJ, local environment, stellar mass, and sSFR, can shed light on this.

The recent mass quenching of lower-mass galaxies ($\log(M_*/M_\odot) \lesssim 10$) might also be partly due to fast-acting stellar and supernova feedback, which is stronger on less massive systems because of their weaker gravitational potential (e.g., Ceverino & Klypin 2009; Hopkins et al. 2014). However, feedback produces short-timescale burstiness in star formation, especially for less massive galaxies (e.g., Hopkins et al. 2014), which is not clearly seen in the median trends in our results. However, part of this discrepancy might be due to different rates for star formation burstiness and quenching. That is, when a galaxy bursts, it almost instantly becomes blue, but the quenching phase takes longer to act. Therefore, the average in bins of M_* -sSFR would be quenching because of this asymmetry. Rapid AGN feedback on less massive galaxies can also have some effect in their quenching (Smethurst et al. 2017).

The higher quenching of our high- z sample compared to SDSS, even at fixed M_* , sSFR, and environment, might be due to a faster and more efficient quenching rate at higher redshifts. By studying a large sample of transiting galaxies at $z \sim 1$, Gonçalves et al. (2012) showed that mass flux from the blue cloud to the red sequence (through the green valley) is larger at $z \sim 1$ compared to the same quantity in the local universe (Martin et al. 2007). The faster quenching rate of transiting galaxies at $z \sim 1$ has been recently reconfirmed by Nogueira-Cavalcante et al. (2018). In this paper, however, we find that this seems to be true for all galaxies (not just transiting systems) and even satellites and centrals. Quenching, regardless of the process, is stronger at $z \sim 1$ for all galaxies at all stellar masses, sSFRs, and Σ s. In agreement with our results, Tinker & Wetzel (2010) and Quadri et al. (2012) showed that satellite quenching must proceed faster at high redshift. Moreover, McGee et al. (2014) argued that given the strong redshift evolution of the SFR, the quenching timescales should be shorter at higher redshift. Recently, Rowlands et al. (2018) also found a faster quenching at $z \sim 0.7$ than the local universe.

Out to $z \sim 1$, the local environment seems to have a milder effect (if any) on the SFA and SFJ, with stellar mass (and sSFR) being the dominant factor over a large range of M_* , Σ , sSFR, and redshift. The dominance of “mass quenching” over “environmental quenching” has been found, particularly for more massive galaxies and at higher redshifts (e.g., Peng et al. 2010; Darvish et al. 2016; Smethurst et al. 2017). Only very dense environments seem to significantly influence the SFA, particularly for the least massive satellites. Ram-pressure stripping and other environmentally driven processes that are practically effective on less massive galaxies might be causing this, whereas mergers are likely behind the trends for more massive galaxies in the field.

The milder (lack of) environmental effects on SFA and SFJ might also be due to the typical long timescales of environmental quenching due to, e.g., strangulation (e.g., Balogh et al. 2000; Peng et al. 2015). However, there is no agreement on the timescales either, as some studies found a short environmental quenching timescale, particularly for less massive satellites (e.g., Boselli et al. 2008; Peng et al. 2010; Crossett et al. 2017; Darvish et al. 2017). In addition, simulations of group and cluster galaxies by Bahé & McCarthy (2015) show that ram-pressure stripping is more effective at $z \sim 1$ than $z = 0$, in agreement with a higher SFA we find for our high- z sample compared to that of the local universe at a fixed local environment. We further note that our results indicate that mass quenching likely happens in short timescales, while the opposite is likely true for environmental quenching (at least when averaged over the whole population). That threshold, established by our methodology (especially given the lack of the SFJ at slightly longer timescales), might set an interesting comparison basis for future studies. Further studies using a modified SFA measure derived over a long timescale are needed to investigate this.

Using the Martin et al. (2017) method, in the future, we will use other physical parameters such as age, gas mass, and gas/stellar metallicity and define new parameters (such as derivatives of SFA over different timescales) to resolve some of the issues stated here and perform new studies that would potentially shed light on the physics of quenching and bursting in galaxies. Moreover, complementary to the LEGA-C survey, high-S/N continuum spectroscopy of (particularly) low-mass galaxies ($\log(M_*/M_\odot) \lesssim 10$) located in very dense environments ($\log \Sigma \gtrsim 1$) at $z \sim 1$ is essential to further investigate the potential environmental trends we already found in the local universe.

6. Summary

We study the “quenching” and “bursting” of galaxies as a function of stellar mass (M_*), local environment (Σ), and sSFR using $\sim 123,000$ *GALEX*/SDSS galaxies at $z \approx 0.02$ – 0.12 and ~ 420 *GALEX*/COSMOS/LEGA-C galaxies at $z \approx 0.6$ – 1.0 with high-S/N continuum spectra. To quantify the recent quenching and bursting of galaxies, we define the SFA and SFJ presented as the time derivative of the extinction-corrected $\text{NUV} - i$ color over the past 300 and 600–300 Myr, respectively (Martin et al. 2017). The key results from this work are as follows.

1. To $z \sim 1$ and at fixed sSFR and Σ , on average, less massive galaxies are quenching, whereas more massive systems are bursting, with a quenching/bursting transition at $\log(M_*/M_\odot) \sim 10.5$ – 11 and likely a short quenching/bursting timescale ($\lesssim 300$ Myr).
2. The bursting of star formation happens mostly in massive ($\log(M_*/M_\odot) \gtrsim 11$), high-sSFR galaxies ($\log(\text{sSFR}/\text{Gyr}^{-1}) \gtrsim -2$), particularly those in the field ($\log(\Sigma/\text{Mpc}^{-2}) \lesssim 0$ and, among group galaxies, satellites more than centrals).
3. Most of the quenching of star formation happens in low-mass ($\log(M_*/M_\odot) \lesssim 9$), low-sSFR galaxies ($\log(\text{sSFR}/\text{Gyr}^{-1}) \lesssim -2$), in particular those located in dense environments ($\log(\Sigma/\text{Mpc}^{-2}) \gtrsim 1$). For central galaxies, quenching is significant even for massive systems. These

show the combined effects of M_* and Σ in the quenching/bursting of galaxies since $z \sim 1$.

4. Stellar mass seems to have stronger effects than local environment on the recent quenching/bursting of galaxies to $z \sim 1$.
5. The strength of mass and environmental quenching/bursting is larger at higher redshifts. Quenching, regardless of its nature, is stronger at higher redshifts.
6. Among group galaxies and at any given M_* , sSFR, and Σ , centrals are quencher (quenching faster) than satellites in an average sense.

Since the LEGA-C survey is not designed a priori to target galaxies in dense environments, complementary to the LEGA-C survey, high-S/N continuum spectroscopy of (particularly) low-mass galaxies ($\log(M_*/M_\odot) \lesssim 10$) located in very dense environments ($\log \Sigma \gtrsim 1$) at $z \sim 1$ is necessary to further investigate and more robustly constrain the potential environmental trends we already found in this work.

We are immensely grateful to the anonymous referee for reading the manuscript and providing very useful comments that improved the quality of this paper. We would like to gratefully thank the LEGA-C team for providing the catalog of spectral indices that was used to compare with the extracted indices for sanity checks. B.D. acknowledges financial support from NASA through the Astrophysics Data Analysis Program (ADAP), grant number NNX12AE20G, and the National Science Foundation, grant number 1716907. B.D. is grateful to Alessandro Rettura for the thoughtful discussions and Mark Seibert for providing further information regarding the available *GALEX* data. D.S. acknowledges financial support from the Netherlands Organisation for Scientific Research (NWO) through a Veni fellowship and from Lancaster University through an Early Career Internal Grant A100679. Based on data products from observations made with ESO telescopes at the La Silla Paranal Observatory under program ID 194.A-2005(A-F). The *Galaxy Evolution Explorer (GALEX)* is a NASA Small Explorer launched in 2003 April. We gratefully acknowledge NASA’s support for construction, operation, and science analysis for the *GALEX* mission, developed in cooperation with the Centre National d’Etudes Spatiales of France and the Korean Ministry of Science and Technology. Funding for SDSS-III has been provided by the Alfred P. Sloan Foundation, the Participating Institutions, the National Science Foundation, and the U.S. Department of Energy Office of Science. The SDSS-III website is <http://www.sdss3.org/>. SDSS-III is managed by the Astrophysical Research Consortium for the Participating Institutions of the SDSS-III Collaboration, including the University of Arizona, the Brazilian Participation Group, Brookhaven National Laboratory, Carnegie Mellon University, the University of Florida, the French Participation Group, the German Participation Group, Harvard University, the Instituto de Astrofísica de Canarias, the Michigan State/Notre Dame/JINA Participation Group, Johns Hopkins University, Lawrence Berkeley National Laboratory, Max Planck Institute for Astrophysics, Max Planck Institute for Extraterrestrial Physics, New Mexico State University, New York University, Ohio State University, Pennsylvania State University, the University of Portsmouth, Princeton University, the Spanish Participation Group, the University of Tokyo, the University of Utah, Vanderbilt

University, the University of Virginia, the University of Washington, and Yale University.

Appendix A

Completeness Corrections for the Local Universe Sample

The SDSS spectroscopic sample has an incompleteness associated with magnitude and the mechanical restrictions due to fiber collision that does not allow us to obtain redshifts for all the galaxies that are closer than $55''$ on the sky. This results in significant spectroscopic incompleteness in crowded regions of the sky, such as galaxy clusters and groups, that are very important in this study. We estimate the magnitude and fiber collision-related completeness by comparing our primary spectroscopic sample (sample A) with the main galaxy sample used to select targets for spectroscopy (Strauss et al. 2002). Similar to Baldry et al. (2006), we divide galaxies in the main galaxy sample into classes based on their magnitude and the number of neighbors within $55''$ (zero, one, and greater than one). The spectroscopic completeness, C , for a class is determined by the number of available spectra divided by the total number of objects in each class.

Figure 13 shows the completeness as a function of Petrosian magnitude r for galaxies with zero, one, and greater than one neighbors within $55''$. As expected, the spectroscopic completeness is higher for galaxies with no neighbors within $55''$, and this comprises the majority of our spectroscopic sample ($\sim 89\%$). Only $\sim 9\%$ and $\sim 2\%$ of our main spectroscopic sample includes galaxies with one and greater than one neighbor within $55''$, respectively. The spectroscopic sample is $>95\%$ complete at $r \gtrsim 15.3$ for galaxies with no neighbors within $55''$, and that comprises the majority of our primary sample ($\sim 86\%$). We weight the estimated local density of galaxies by $1/C$ to take the spectroscopic incompleteness due to magnitude and fiber collision into account.

Since we use a flux-limited spectroscopic sample ($r \leq 17.7$), we need to compensate for the decrease in the number density of galaxies with increasing redshift when estimating the local density of galaxies. Otherwise, we unrealistically underestimate the local density of galaxies at higher redshifts. As we explained in Section 3.1.1, we model the change in the mean number of galaxies (in redshift bins of $\Delta z = 0.005$) as a function of redshift with

$$N(z)dz = Az^2e^{-(z/z_c)^\alpha} dz, \quad (5)$$

According to Equation (5), the mean number of galaxies increases with increasing redshift as z^2 as we cover a larger spatial volume, and, at the same time, it decreases with the selection function ($\Psi = e^{-(z/z_c)^\alpha}$), since the intrinsically fainter galaxies are no longer observable at higher redshifts. Figure 14(a) shows the redshift distribution of the data and the best-fit model given by $A = (8.50 \pm 0.75) \times 10^6$, $z_c = 0.0653 \pm 0.0035$, and $\alpha = 1.417 \pm 0.054$. We correct the local density of each galaxy by a weight $1/\Psi(z)$. Figure 14(b) shows the selection function as a function of redshift. In order to avoid large uncertainties and fluctuations in the estimated densities due to a smaller sample size at higher redshifts, we only use galaxies for which $\Psi(z) \geq 0.1$. This corresponds to $z \sim 0.12$. We also define a lower redshift cut of $z = 0.02$ to avoid issues related to local motions, edge effects, and the photometry of very bright, nearby sources.

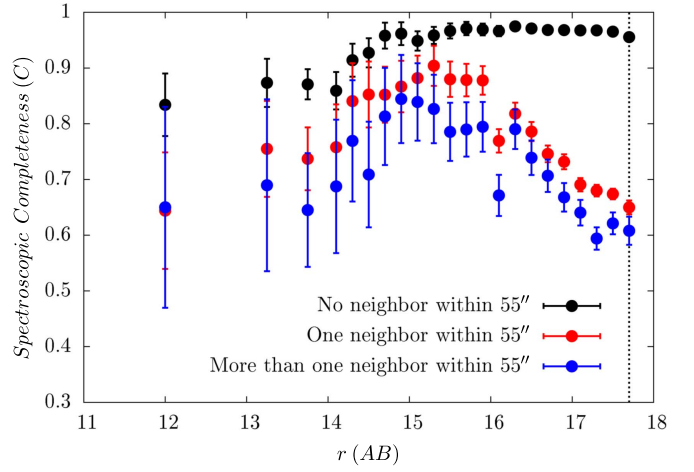


Figure 13. Spectroscopic completeness as a function of Petrosian magnitude r for galaxies with zero, one, and greater than one neighbors within $55''$. The vertical dotted line shows the magnitude limit used for sample selection ($r \leq 17.7$). Beyond this, spectroscopic completeness decreases significantly. The uncertainties are Poissonian.

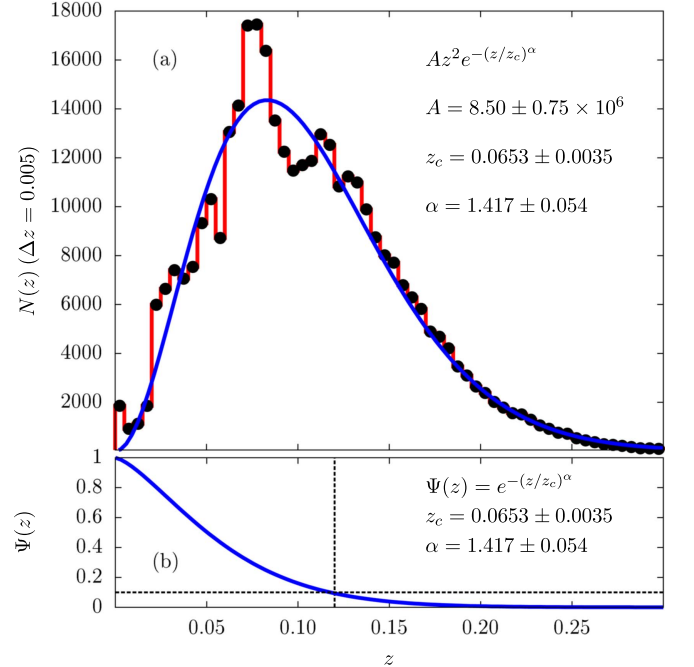


Figure 14. (a) Spectroscopic redshift distribution of the local universe data (in bins of $\Delta z = 0.005$; red histogram) and the best-fit model ($z^2 e^{-(z/z_c)^\alpha}$; blue solid curve) given by $A = (8.50 \pm 0.75) \times 10^6$, $z_c = 0.0653 \pm 0.0035$, and $\alpha = 1.417 \pm 0.054$. (b) Selection function (Ψ) as a function of redshift. The horizontal dashed line shows where $\Psi = 0.1$. This approximately corresponds to $z = 0.12$, indicated by the vertical dashed line.

The performance of the nearest-neighbor method used in Section 3.1.1 depends on the selection of the value N (n th nearest neighbor), as discussed in Darvish et al. (2015b). A small value may result in unrealistically large local densities because of Poisson noise and random clustering of spatially uncorrelated galaxies, whereas a large value tends to over-smooth the details of galaxy distribution and is prone to underestimation of local densities. We compare estimated surface densities using 4th, 5th, and 10th nearest-neighbor methods as shown in Figure 15. The median absolute deviation

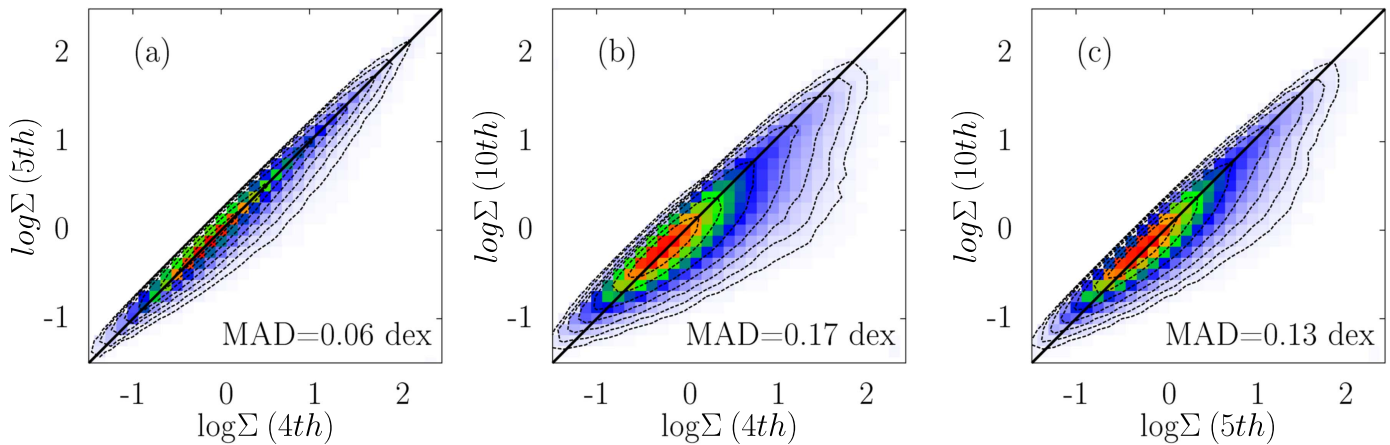


Figure 15. Comparison between the estimated surface densities using the (a) 4th and 5th, (b) 4th and 10th, and (c) 5th and 10th nearest-neighbor methods. The median absolute deviation (MAD) between the density values is also shown. There is an overall good agreement between the estimated densities, with only 0.3% (4th and 5th), 2.7% (4th and 10th), and 1.2% (5th and 10th) of the sources more than 1 dex different in density.

between density values of the 4th and 5th, 4th and 10th, and 5th and 10th methods are 0.06, 0.17, and 0.13 dex, respectively. Only 0.3%, 2.7%, and 1.2% of the sources are more than 1 dex different in density value when we compare the 4th and 5th, 4th and 10th, and 5th and 10th estimations, respectively. However, we note that the density estimations are slightly biased toward higher values for lower n th estimators due to the nature of the nearest-neighbor method. Darvish et al. (2015b) performed two sets of simulations, comparing the performance of different density estimators. Both sets of simulations show that the 10th nearest neighbor outperforms the 5th nearest-neighbor method. Hence, we use $N = 10$ in Section 3.1.1.

Another parameter that affects the estimated surface densities in Section 3.1.1 is Δv . A small value of Δv underestimates the surface densities in dense regions due to the finger-of-god effect, whereas a large value affects the low surface densities. Here we use $\Delta v = \pm 1000 \text{ km s}^{-1}$, which is equivalent to the typical radial velocity dispersion of rich galaxy clusters and is large enough to suppress the finger-of-god effect. Moreover, Cooper et al. (2005) showed that a velocity range of $\pm 1000\text{--}1500 \text{ km s}^{-1}$ is best suited for environmental studies in a broad range of environments.

Appendix B

Adaptive Kernel versus 10th Nearest Neighbor

Using different density estimators in the local universe (projected distance to the 10th nearest neighbor) and high- z (adaptive kernel smoothing) might lead to a bias when we compare the results at low and high redshift. To investigate this, we perform the density estimation using the 10th nearest-neighbor method for our high- z sample as well and compare it with that of adaptive kernel smoothing. Figure 16 shows the comparison. We find a relatively good agreement between the two, with a median offset of ~ 0.07 dex ($\log \Sigma(\text{Kernel}) - \log \Sigma(10\text{th})$) and a median absolute deviation of ~ 0.14 dex. Therefore, the selection of different density estimators does not have significant effects in the presented results.

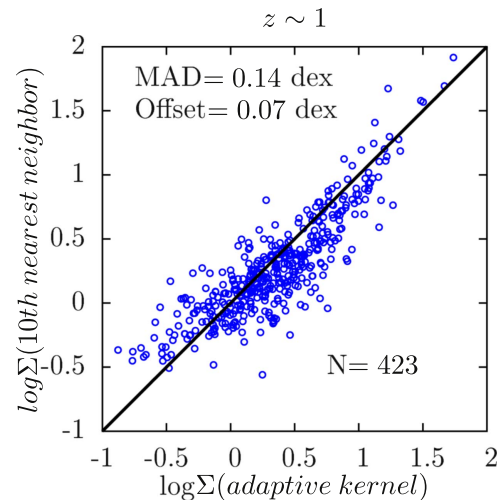


Figure 16. Comparison between the estimated surface densities using the distance to the 10th nearest neighbor and the adaptive kernel smoothing methods for our high- z sample. The median offset and median absolute deviation (MAD) between the density values are also shown. We find an overall good agreement between the two methods.

Appendix C

Comparison

Martin et al. (2017) performed a comparison between some physical parameters and trends based on their method and those in the literature at $z \sim 0$ and found a relatively good agreement, with small offsets and deviations. Here we present two more comparisons, highlighting the robustness and reliability of the method.

Figure 17(a) shows the comparison between the atomic hydrogen mass (M_{HI}) measurements from the ALFALFA survey (Haynes et al. 2011) and estimations based on the Martin et al. (2017) methodology for 5344 sources matched with our local universe sample. Note that Martin et al. (2017)

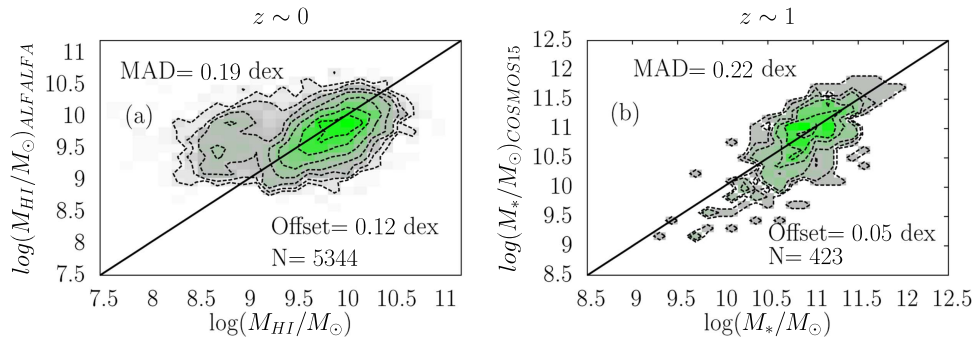


Figure 17. (a) Comparison between the atomic hydrogen mass M_{HI} measurements from the ALFALFA survey (Haynes et al. 2011) and estimations based on the Martin et al. (2017) methodology for 5344 sources matched with our local universe sample. There is a good agreement between the two at $\log(M_{\text{HI}}/M_{\odot}) \gtrsim 9$, with an offset and a median absolute deviation of ~ 0.1 and 0.2 dex, respectively. (b) Comparison between the stellar masses from the COSMOS15 catalog (Laigle et al. 2016) and those estimated for our high- z LEGA-C sample at $z \sim 1$ using the Martin et al. (2017) method. Only a small offset of ~ 0.05 and a median absolute deviation of ~ 0.2 are seen between the two.

gives the total cold gas mass including atomic hydrogen (HI), molecular hydrogen (H_2), helium (He), and a small fraction of metals. We convert the total gas mass to M_{HI} assuming that the composition of the cold gas in the local universe is 59% HI, 15% H_2 , and 26% He and metals (Obreschcow & Rawlings 2009). According to Figure 17(a), for $\log(M_{\text{HI}}/M_{\odot}) \gtrsim 9$, there is a good agreement between the two, with a small offset of ~ 0.1 dex and a median absolute deviation of ~ 0.2 dex. Note that part of the dispersion might be due to the mass and galaxy-type dependence of the $M_{\text{H}_2}/M_{\text{HI}}$ ratio. The cause of the offset and the disagreement at low masses ($\log(M_{\text{HI}}/M_{\odot}) \lesssim 9$) is beyond the scope of this work.

Figure 17(b) compares the stellar masses from the COSMOS15 catalog (Laigle et al. 2016) and those estimated for our high- z LEGA-C sample at $z \sim 1$ using the Martin et al. (2017) method. Only a small offset of ~ 0.05 and a median absolute deviation of ~ 0.2 are seen between the two, indicating that the methodology used here gives reasonable physical values even at higher redshifts.

Appendix D

High- z Results Using Groups with >10 Members

In presenting the high- z sample results, in order to increase the sample size and a broader range of the physical parameters involved (M_* , Σ , and sSFR), all groups with ≥ 2 members are considered. This is different than our low- z sample selection, where groups with >10 members are considered. In addition to potential biases that might arise when comparing the low- and high-redshift samples, this selection of high- z samples (all groups with ≥ 2 members) makes it more vulnerable to contamination by interlopers. We check whether we can still recover the global trends between SFA (or SFJ), M_* , and Σ for our high- z sample by choosing all group galaxies whose groups have >10 members. This leads to a factor of ~ 2 and ~ 9 reduction in the number of satellites and centrals, respectively. However, as shown in Figure 18, even with this limited sample size, we can retrieve the trends that are already shown in Section 4.2 and Figure 7. Therefore, the presented results are likely not much affected by selecting ≥ 2 group membership for our high- z sample.

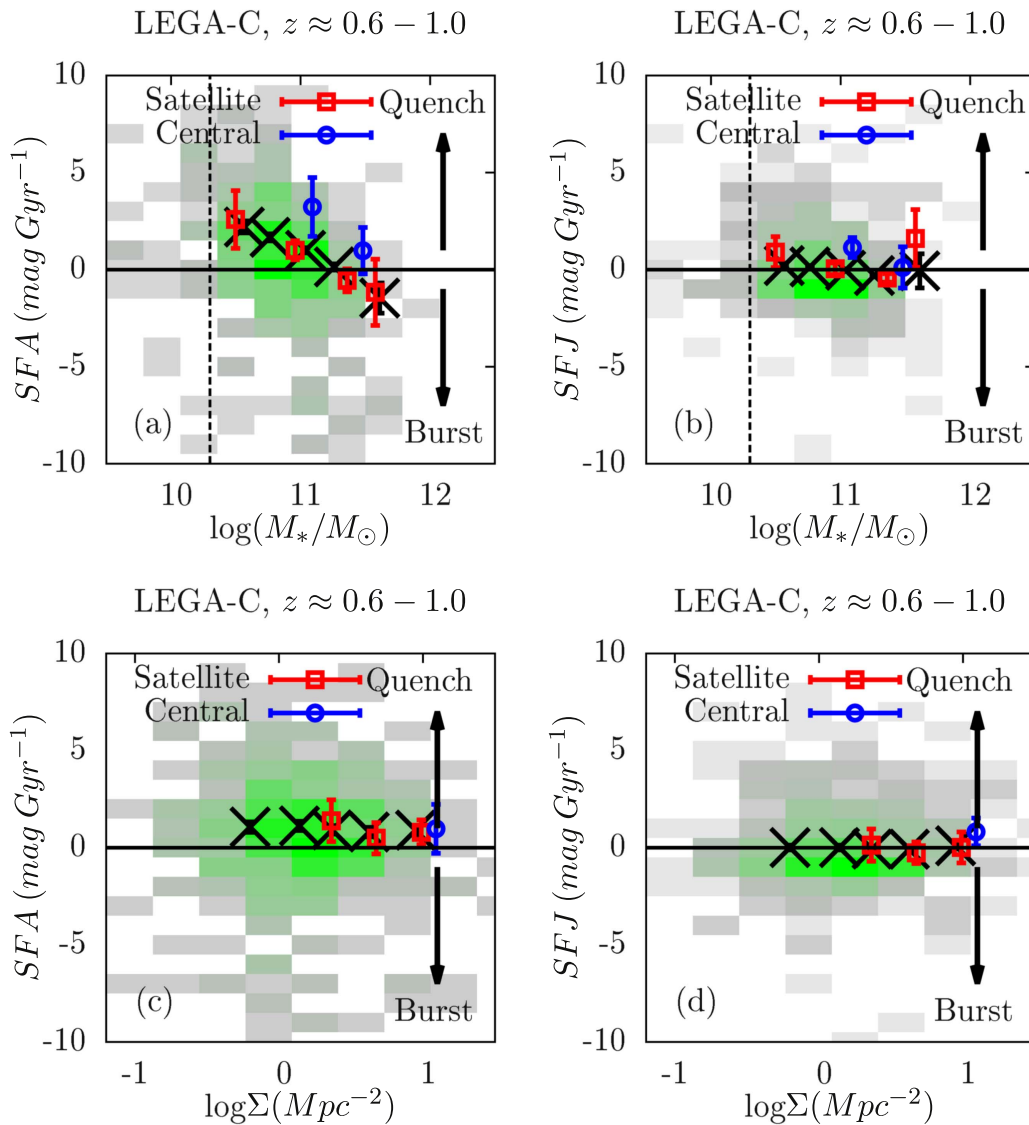


Figure 18. Similar to Figure 7 for the LEGA-C high- z sample at $z \sim 1$ but for group galaxies whose groups have >10 members. Red, blue, and black points show the median values for satellite, central, and all galaxies. Similar to Figure 7, we can still retrieve the trends between SFA (or SFJ), M_* , and Σ for satellites and centrals.

ORCID iDs

Behnam Darvish <https://orcid.org/0000-0003-4919-9017>
 Nick Z. Scoville <https://orcid.org/0000-0002-0438-3323>
 and David Sobral <https://orcid.org/0000-0001-8823-4845>

References

- Alam, S., Albareti, F. D., Allende Prieto, C., et al. 2015, *ApJS*, 219, 12
 Bahé, Y. M., & McCarthy, I. G. 2015, *MNRAS*, 447, 969
 Baldry, I. K., Balogh, M. L., Bower, R. G., et al. 2006, *MNRAS*, 373, 469
 Balogh, M. L., Morris, S. L., Yee, H. K. C., Carlberg, R. G., & Ellingson, E. 1999, *ApJ*, 527, 54
 Balogh, M. L., Navarro, J. F., & Morris, S. L. 2000, *ApJ*, 540, 113
 Bekki, K., & Couch, W. J. 2003, *ApJL*, 596, L13
 Berti, A. M., Coil, A. L., Behroozi, P. S., et al. 2017, *ApJ*, 834, 87
 Best, P. N., Kauffmann, G., Heckman, T. M., et al. 2005, *MNRAS*, 362, 25
 Birnboim, Y., & Dekel, A. 2003, *MNRAS*, 345, 349
 Bluck, A. F. L., Mendel, J. T., Ellison, S. L., et al. 2014, *MNRAS*, 441, 599
 Boselli, A., Boissier, S., Cortese, L., & Gavazzi, G. 2008, *ApJ*, 674, 742
 Boselli, A., & Gavazzi, G. 2006, *PASP*, 118, 517
 Boselli, A., & Gavazzi, G. 2014, *A&ARv*, 22, 74
 Bruzual, G., & Charlot, S. 2003, *MNRAS*, 344, 1000
 Capak, P., Aussel, H., Ajiki, M., et al. 2007, *ApJS*, 172, 99
 Catinella, B., Schiminovich, D., Cortese, L., et al. 2013, *MNRAS*, 436, 34
 Ceverino, D., & Klypin, A. 2009, *ApJ*, 695, 292
 Chilingarian, I. V., Melchior, A.-L., & Zolotukhin, I. Y. 2010, *MNRAS*, 405, 1409
 Chilingarian, I. V., & Zolotukhin, I. Y. 2012, *MNRAS*, 419, 1727
 Cooper, M. C., Newman, J. A., Madgwick, D. S., et al. 2005, *ApJ*, 634, 833
 Cortese, L., & Hughes, T. M. 2009, *MNRAS*, 400, 1225
 Crossett, J. P., Pimbblet, K. A., Jones, D. H., Brown, M. J. I., & Stott, J. P. 2017, *MNRAS*, 464, 480
 Croton, D. J., Springel, V., White, S. D. M., et al. 2006, *MNRAS*, 365, 11
 Darvish, B., Mobasher, B., Martin, D. C., et al. 2017, *ApJ*, 837, 16
 Darvish, B., Mobasher, B., Sobral, D., et al. 2015a, *ApJ*, 814, 84
 Darvish, B., Mobasher, B., Sobral, D., et al. 2016, *ApJ*, 825, 113
 Darvish, B., Mobasher, B., Sobral, D., Scoville, N., & Aragon-Calvo, M. 2015b, *ApJ*, 805, 121
 Darvish, B., Sobral, D., Mobasher, B., et al. 2014, *ApJ*, 796, 51
 Davidzon, I., Cucciati, O., Bolzonella, M., et al. 2016, *A&A*, 586, A23
 De Lucia, G., Springel, V., White, S. D. M., Croton, D., & Kauffmann, G. 2006, *MNRAS*, 366, 499
 Dekel, A., Zolotov, A., Tweed, D., et al. 2013, *MNRAS*, 435, 999
 Duarte, M., & Mamon, G. A. 2014, *MNRAS*, 440, 1763
 Duivenvoorden, S., Oliver, S., Buat, V., et al. 2016, *MNRAS*, 462, 277
 Efstathiou, G., & Moody, S. J. 2001, *MNRAS*, 325, 1603
 Ellison, S. L., Mendel, J. T., Patton, D. R., & Scudder, J. M. 2013, *MNRAS*, 435, 3627

- Ellison, S. L., Patton, D. R., Simard, L., et al. 2010, *MNRAS*, 407, 1514
- Ellison, S. L., Patton, D. R., Simard, L., & McConnell, A. W. 2008, *AJ*, 135, 1877
- Erfanianfar, G., Popesso, P., Finoguenov, A., et al. 2016, *MNRAS*, 455, 2839
- Fabello, S., Kauffmann, G., Catinella, B., et al. 2012, *MNRAS*, 427, 2841
- Fabian, A. C. 2012, *ARA&A*, 50, 455
- Fang, J. J., Faber, S. M., Koo, D. C., & Dekel, A. 2013, *ApJ*, 776, 63
- Finoguenov, A., Guzzo, L., Hasinger, G., et al. 2007, *ApJS*, 172, 182
- Fitzpatrick, P. J., & Graves, G. J. 2015, *MNRAS*, 447, 1383
- Gaibler, V., Khochfar, S., Krause, M., & Silk, J. 2012, *MNRAS*, 425, 438
- Gonçalves, T. S., Martin, D. C., Menéndez-Delmestre, K., Wyder, T. K., & Koekemoer, A. 2012, *ApJ*, 759, 67
- Guo, Y., Bell, E. F., Lu, Y., et al. 2017, *ApJL*, 841, L22
- Gürkan, G., Hardcastle, M. J., Jarvis, M. J., et al. 2015, *MNRAS*, 452, 3776
- Guzzo, L., Cassata, P., Finoguenov, A., et al. 2007, *ApJS*, 172, 254
- Haines, C. P., Pereira, M. J., Smith, G. P., et al. 2013, *ApJ*, 775, 126
- Hatfield, P. W., & Jarvis, M. J. 2017, *MNRAS*, 472, 3570
- Haynes, M. P., Giovanelli, R., Martin, A. M., et al. 2011, *AJ*, 142, 170
- Henriques, B. M. B., White, S. D. M., Thomas, P. A., et al. 2017, *MNRAS*, 469, 2626
- Hopkins, P. F., & Elvis, M. 2010, *MNRAS*, 401, 7
- Hopkins, P. F., Kereš, D., Oñorbe, J., et al. 2014, *MNRAS*, 445, 581
- Huchra, J. P., & Geller, M. J. 1982, *ApJ*, 257, 423
- Hung, C.-L., Casey, C. M., Chiang, Y.-K., et al. 2016, *ApJ*, 826, 130
- Ilbert, O., Capak, P., Salvato, M., et al. 2009, *ApJ*, 690, 1236
- Kalfountzou, E., Stevens, J. A., Jarvis, M. J., et al. 2017, *MNRAS*, 471, 28
- Kauffmann, G., Heckman, T. M., White, S. D. M., et al. 2003, *MNRAS*, 341, 33
- Kawinwanichakij, L., Papovich, C., Quadri, R. F., et al. 2017, *ApJ*, 847, 134
- Kewley, L. J., Geller, M. J., & Barton, E. J. 2006, *AJ*, 131, 2004
- Kovač, K., Lilly, S. J., Knobel, C., et al. 2014, *MNRAS*, 438, 717
- Koyama, Y., Smail, I., Kurk, J., et al. 2013, *MNRAS*, 434, 423
- Laigle, C., McCracken, H. J., Ilbert, O., et al. 2016, *ApJS*, 224, 24
- Lee, S.-K., Im, M., Kim, J.-W., et al. 2015, *ApJ*, 810, 90
- Lidman, C., Suherli, J., Muzzin, A., et al. 2012, *MNRAS*, 427, 550
- Lin, L., Cooper, M. C., Jian, H.-Y., et al. 2010, *ApJ*, 718, 1158
- Martig, M., Bournaud, F., Teyssier, R., & Dekel, A. 2009, *ApJ*, 707, 250
- Martin, D. C., Fanson, J., Schiminovich, D., et al. 2005, *ApJL*, 619, L1
- Martin, D. C., Gonçalves, T. S., Darvish, B., Seibert, M., & Schiminovich, D. 2017, *ApJ*, 842, 20
- Martin, D. C., Wyder, T. K., Schiminovich, D., et al. 2007, *ApJS*, 173, 342
- McGee, S. L., Bower, R. G., & Balogh, M. L. 2014, *MNRAS*, 442, L105
- McIntosh, D. H., Guo, Y., Hertzberg, J., et al. 2008, *MNRAS*, 388, 1537
- Mihos, J. C., & Hernquist, L. 1996, *ApJ*, 464, 641
- Mihos, J. C., Richstone, D. O., & Bothun, G. D. 1992, *ApJ*, 400, 153
- Mortazavi, S. A., Lotz, J. M., Barnes, J. E., Privon, G. C., & Snyder, G. F. 2018, *MNRAS*, 474, 3423
- Muldrew, S. I., Croton, D. J., Skibba, R. A., et al. 2012, *MNRAS*, 419, 2670
- Nantais, J. B., Muzzin, A., van der Burg, R. F. J., et al. 2017, *MNRAS*, 465, L104
- Noeske, K. G., Weiner, B. J., Faber, S. M., et al. 2007, *ApJL*, 660, L43
- Nogueira-Cavalcante, J. P., Gonçalves, T. S., Menéndez-Delmestre, K., & Sheth, K. 2018, *MNRAS*, 473, 1346
- Obreschkow, D., & Rawlings, S. 2009, *MNRAS*, 394, 1857
- Pasquali, A., Gallazzi, A., Fontanot, F., et al. 2010, *MNRAS*, 407, 937
- Patel, S. G., Holden, B. P., Kelson, D. D., Illingworth, G. D., & Franx, M. 2009, *ApJL*, 705, L67
- Patel, S. G., Kelson, D. D., Holden, B. P., Franx, M., & Illingworth, G. D. 2011, *ApJ*, 735, 53
- Patton, D. R., & Atfield, J. E. 2008, *ApJ*, 685, 235
- Peng, Y., Maiolino, R., & Cochrane, R. 2015, *Natur*, 521, 192
- Peng, Y.-j., Lilly, S. J., Kovač, K., et al. 2010, *ApJ*, 721, 193
- Peng, Y.-j., Lilly, S. J., Renzini, A., & Carollo, M. 2012, *ApJ*, 757, 4
- Perez, J., Tissera, P., Padilla, N., Alonso, M. S., & Lambas, D. G. 2009, *MNRAS*, 399, 1157
- Poggianti, B. M., Fasano, G., Omizzolo, A., et al. 2016, *AJ*, 151, 78
- Poggianti, B. M., Jaffé, Y. L., Moretti, A., et al. 2017, *Natur*, 548, 304
- Pozzetti, L., Bolzonella, M., Zucca, E., et al. 2010, *A&A*, 523, A13
- Quadri, R. F., Williams, R. J., Franx, M., & Hildebrandt, H. 2012, *ApJ*, 744, 88
- Robotham, A. S. G., Driver, S. P., Davies, L. J. M., et al. 2014, *MNRAS*, 444, 3986
- Rowlands, K., Wild, V., Bourne, N., et al. 2018, *MNRAS*, 473, 1168
- Salpeter, E. E. 1955, *ApJ*, 121, 161
- Scoville, N., Arnouts, S., Aussel, H., et al. 2013, *ApJS*, 206, 3
- Scoville, N., Aussel, H., Brusa, M., et al. 2007, *ApJS*, 172, 1
- Seibert, M., Wyder, T., Neill, J., et al. 2012, American Astronomical Society Meeting Abstracts, 219, 340.01
- Shankar, F., Buchan, S., Rettura, A., et al. 2015, *ApJ*, 802, 73
- Sheth, K., Vogel, S. N., Regan, M. W., Thornley, M. D., & Teuben, P. J. 2005, *ApJ*, 632, 217
- Shivaei, I., Reddy, N. A., Shapley, A. E., et al. 2015, *ApJ*, 815, 98
- Silk, J., & Nusser, A. 2010, *ApJ*, 725, 556
- Smethurst, R. J., Lintott, C. J., Bamford, S. P., et al. 2017, *MNRAS*, 469, 3670
- Sobral, D., Best, P. N., Smail, I., et al. 2011, *MNRAS*, 411, 675
- Sobral, D., Stroe, A., Dawson, W. A., et al. 2015, *MNRAS*, 450, 630
- Somerville, R. S., Hopkins, P. F., Cox, T. J., Robertson, B. E., & Hernquist, L. 2008, *MNRAS*, 391, 481
- Speagle, J. S., Steinhardt, C. L., Capak, P. L., & Silverman, J. D. 2014, *ApJS*, 214, 15
- Springel, V., White, S. D. M., Jenkins, A., et al. 2005, *Natur*, 435, 629
- Strauss, M. A., Weinberg, D. H., Lupton, R. H., et al. 2002, *AJ*, 124, 1810
- Stroe, A., Sobral, D., Dawson, W., et al. 2015, *MNRAS*, 450, 646
- Tinker, J. L., & Wetzel, A. R. 2010, *ApJ*, 719, 88
- Tonnesen, S., & Cen, R. 2012, *MNRAS*, 425, 2313
- van de Voort, F., Bahé, Y. M., Bower, R. G., et al. 2017, *MNRAS*, 466, 3460
- van der Wel, A., Noeske, K., Bezanson, R., et al. 2016, *ApJS*, 223, 29
- Vulcani, B., Poggianti, B. M., Finn, R. A., et al. 2010, *ApJL*, 710, L1
- Wagner, A. Y., Bicknell, G. V., & Umemura, M. 2012, *ApJ*, 757, 136
- Wetzel, A. R., Tinker, J. L., Conroy, C., & van den Bosch, F. C. 2014, *MNRAS*, 439, 2687
- Whitaker, K. E., van Dokkum, P. G., Brammer, G., & Franx, M. 2012, *ApJL*, 754, L29
- Wuyts, S., Förster Schreiber, N. M., van der Wel, A., et al. 2011, *ApJ*, 742, 96
- Xu, C. K., Zhao, Y., Scoville, N., et al. 2012, *ApJ*, 747, 85
- Zamojski, M. A., Schiminovich, D., Rich, R. M., et al. 2007, *ApJS*, 172, 468